Comprehensive Design and Prototype of VLC Receivers with Large Detection Areas

Pooya Nabavi and Murat Yuksel

***Abstract*—Stable and practical reception of visible light communication (VLC) signals at mobile devices necessitates opto-electronic receivers with large detection areas to attain wide field-of-view (FOV) as well as robustness against blockage. However, large detection (or aperture) area reduces the effective bandwidth of VLC receivers. We design and prototype a VLC receiver with multi-photodetector array followed by a multi-stage amplifier, capable of attaining high-speed data rates for white phosphorous LED light. The receiver array can be arranged conformal to the surface shape of mobile devices. We test the VLC system's performance under vibrations, characterize delay spread arising from movements and wide FOV of the receiver, design multi-symbol detection techniques based on time and spatial reception diversity, and evaluate the performance with real data transmissions.**

***Index Terms*—Indoor visible light communications, System design, Vibrant VLC link, Multiple-symbol detection, Adaptive Decision Feedback Affine Projection Algorithm.**

I. Introduction

OPTICAL wireless systems have the potential to provide high-speed, cost-effective, and secure wireless communications in indoor environments [2], [3] as well as free-space [4], [5], and even in underwater [6]–[8]. As living spaces are getting populated with more densely deployed wireless devices, traditional licensed radio frequency (RF) bands are becoming scarcer and costlier. Moreover, the interference from omni-directional RF signals limits the scalability of wireless network throughput to sub-linear increase only [9], [10]. To increase the aggregate wireless throughput, system designs using suitable electromagnetic spectrum bands that allow more spatial reuse are urgently needed.

Due to their inherent directionality, optical bands (i.e., wavelengths ranging approximately from 100 nm to 1 mm) are open to high spatial reuse. Since they do not interfere with legacy RF bands, the optical bands provide complementary wireless channels which can respond to the spectrum crunch. As a special case of optical wireless communications, Visible Light Communication (VLC) uses the visible band with wavelengths in 400-700 nm. VLC has a great potential for real use as it can utilize Light Emitting Diodes (LEDs) that are becoming widely available for lighting via solid-state technologies. VLC can play an important role in the emerging 5G wireless systems by coexisting with WiFi [11] and providing high-speed indoor access. Further, VLC can enable localization and access applications in GPS- or RF-challenged environments such as asset tracking [12] in a hospital or inventory monitoring in a supermarket. It can also contribute to smart city applications such as road safety systems [13] and autonomous vehicles.

Wireless community has recognized this potential and has recently made significant efforts in exploring VLC technologies. Although VLC offers a very promising approach to attaining high speed indoor wireless networking, a typical indoor environment includes dynamics detrimental to VLC performance. The mobility and vibrations produced by a typical indoor setting (e.g., a simple shake from typing on a laptop or movements of smartphone while talking or watching video) negatively affect a VLC receiver's signal reception. These casual human actions may result in attenuation and cause a time dependent inter-symbol interference (ISI) on the VLC channel, and thus limit the effective transfer rate and range of indoor VLC systems. These impairments necessitate the design of intelligent receivers as well as efficient transmission techniques. To the best of our knowledge, the negative effects of the phenomena above on the indoor VLC system performance and effective solutions for them have not yet been explored, which is the main focus of our work.

In our preliminary work [1], we introduced a multi-stage amplifier design followed by a symbol detection mechanism that accounts for impairments in the indoor VLC. This manuscript extends our study with more design choices and presents a proof-of-concept prototype with real data transfers. We design and prototype an indoor VLC receiver system with three-stage amplification that attains 20 Mbps transfer at a range of 7 m. Under mobility and intense vibrations, we evaluate the performance of the VLC link in terms of stability and transfer rate. We show the ISI caused by the vibration by measuring the delay spread in the channel, and quantify the reduction in the maximum achievable rate due to the vibration in the receiver's body. In order to tackle the ISI, we design and employ a Multiple-Symbol Detection (MSD) algorithm that optimally remedies the high Bit Error Rate (BER) caused

Pooya Nabavi and Murat Yuksel are with the Department of Electrical and Computer Engineering, University of Central Florida, Orlando, FL, USA (e-mail: pooya.nabavi@knights.ucf.edu and Murat.Yuksel@ucf.edu). Both authors are also affiliated with College of Optics and Photonics (CREOL), University of Central Florida, Orlando, FL, USA.

A preliminary version of this work was published in [1]. this manuscript extends by adding (i) an optimal receiver gain combining technique that uses spatial diversity to attain robustness to vibration, (ii) analytic exploration of the tradeoffs between the number of photodetectors and hardware complexity for receiver combining and performance analysis based on Saddle-Point Approximation method, (iii) significantly more results including real data transmission and reception, (iv) a proof-of-concept prototype and experimental results demonstrating the effectiveness of the proposed VLC receiver and detection algorithms, (v) detailed circuit designs and systematical modeling to calculate receiver capacitance for high-speed VLC receivers, (vi) experimental evaluation of the capabilities of the proposed detection algorithms in real data communication links.

The authors acknowledge the support from U.S. National Science Foundation awards 1663764 and 1836741

by the ISI. Then, to curb MSD's exponential computational complexity, we design an adaptive Decision Feedback Affine Projection Algorithm (DF-APA).

To increase the robustness of VLC receivers against vibrations in their physical structures, we also explore receiver combining techniques. To this end, we evaluate Single Input Multiple Output (SIMO) designs equipped with a novel Optimal Gain Combination (OGC) detection algorithm which takes advantage of the intrinsic spatial diversity of the VLC receivers with large detection area. Note that relying on the extra spatial diversity provided by the SIMO reception is highly necessary in order to achieve the desired reliability in vibrant VLC links. Ultimately, we use the Saddle-Point Approximation (SPA) method to evaluate the BER performance of the SIMO designs and compare them with the optimal MSD method employed in single-receiver systems. We also, using SPA, derive analytic relations for the BER performance of both SISO and SIMO VLC receivers.

A key feature of our VLC receiver its usage of multiple photo-detector (PD) arrays to compose a large detection (or aperture) area. These PDs can be used to cover large reception surfaces in forms conformal to the shape of the receiver device (Fig. 1). As mobile receivers such as smartphones move around, being able to receive at multiple detection areas is a key enabler for adoption of VLC to casual use in mobile systems. Major contributions of our work include:

- A multi-PD array VLC receiver design that can be conformal to surfaces of the shapes of devices such as laptops, smartphones, or virtual reality headsets.
- Modeling of a VLC channel by using empirical data in a casual indoor setting with minor movements such as shake or vibration.
- A three-stage amplification technique that can accommodate delay spread arising from a large aggregate receiver surface area exceeding 5 cm^2 and movements in the receiver body.
- Prototype of an VLC link that is scalable and suitable for an indoor environment, and attains data rates up to 20 Mbps at 7 m distance with BER less than 10^{-5} under intense vibrations in receiver's body, i.e., about 2.5 times per second oscillation over a 4 cm displacement.
- Empirical characterization of delay spread (and hence non-zero memory) in indoor VLC links with wide FOV receivers when vibrations exist in the environment. Formulation of the ISI effects by considering vibration in the environment, beam divergence angle, data rate and link range.
- Optimal and adaptive multi-symbol detection algorithms for tackling the time-dependent ISI of the VLC channel arising from the vibrations or movements.
- An Optimal Gain Combining (OGC) technique for multi-PD VLC receivers that utilize spatial diversity. Comparison of the OGC with the traditional Equal Gain Combining (EGC) for multi-PD receivers.
- Analytical closed-form expression of BER performance for the OGC in multi-PD VLC receivers using SPA.

The rest of the paper is organized as follows: In Section II, we survey the relevant background on the latest available VLC technologies. Furthermore, The proposed methodology, theoretical analysis and the detailed circuit design for proposed VLC receiver and transmitter are described in Sections II and Section III, respectively. We provide the details of the proof-of-concept prototype and analyze the experimental results in Section IV. The proposed detection algorithms are designed in Section V and VI. Section VII illustrates the simulation scenarios and discusses the results. Finally, we summarize and conclude the paper in Section VIII.

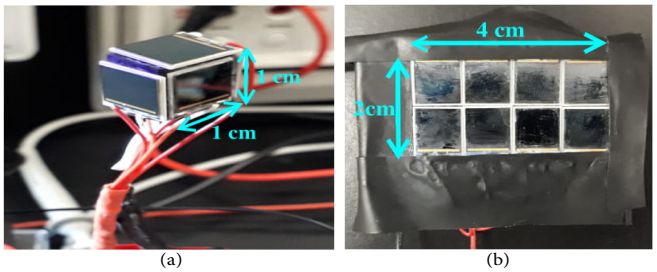

(a) (b)

Fig. 1. Conformal PD structures: (a) Cubical; (b) Flat [1]

II. Related Work

There has been major efforts in VLC receiver design [20]–[22]. However, VLC receivers are still not widely and commercially adopted. Insufficient efficiency to offer both high speeds (tens of Mbps) [15], [16], [23] and long ranges (at least 5 m) [14], [17] are among the major reasons dissuading users to extensively employ these receivers (Fig. 2). Moreover, the limited field of view (FOV) ($\approx 75°$) and detection area ($\approx 1\ \text{mm}^2$) in the existing VLC receivers cause the generated data-carrying photo-current signal to be small and the quality of the data reception to be dependent on the spatial positions of the receiver and transmitter. These limitations make it difficult to broadly implement wide-range VLC systems in environments where the receiving person is constantly on the

TABLE I
Performance Comparison

	R	BW	FOV	Packet Loss Rate
Our Prototype	7.1 m	20 MHz	360°	10^{-6}
Pure LiFi-X [14]	1.8 m	42 MHz	60°	$\approx 3.4 \times 10^{-5}$
[15]	2.4 m	10 KHz	10°	10^{-2}
[16]	50 m	50 KHz	75°	3.2×10^{-4}
Thorlabs [17]	0.45 m	12 MHz	150°	$\approx 10^{-4}$

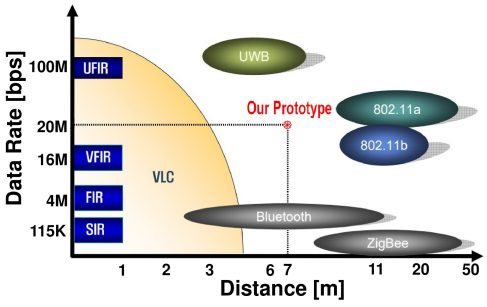

Fig. 2. VLC technology, IEEE 802.15.7 standard [18] [19] [1]

move. Table I details the performance of the state of the art VLC technologies.

For providing proper lighting coverage, the technologies listed in Table I utilize white Phosphorus LEDs (not single wavelength, narrow beam lasers) as their predominant choice for data transmission. These white phosphorous LEDs, which are primarily designed for illumination purposes, typically deploy a blue LED chip plus a phosphor coating which generates the white light. The phosphor has a slow decay time (i.e., recombination lifetime) which limits the effective bandwidth to a few MHz [24], [25]. Filtering of the blue light at the receiver side improves the bandwidth to some extent, however the effective bandwidth is still reduced to less than or equal to 50 MHz [18], [19], [24], [25]. As a result, the maximum transmission bit rate in single career incoherent phosphor-based VLC is limited to maximum 50 Mbps. By utilizing monotonic (single wavelength) narrow beam lasers, GHz speeds are achievable but lasers beams have human safety risks and are too directional for lighting. Hence, these laser-based wireless communication techniques are not comparable to our work in luminescent VLC.

In this paper, by making the VLC receivers conformal, we focus on design and implementation of wide FOV receivers with large aperture area and show a maximum transmission rate of 20 Mbps at a range of 7 m. As discussed in the following sections, the quality of the received signal in the designed system is, to a great extent, independent of the spatial positions of the receiver and transmitter due to its large aggregate active detection surface (or aperture) area and omni-directional reception.

III. VLC Receiver with Large Aperture Area

Design of a cost effective and conformal VLC receiver involves (1) selecting an appropriate PD with *large active area* while keeping its operational bandwidth high (which also translates to lower rise/response time) and eliminating additional noise due to enlarged area, (2) designing a stable amplification circuitry that considers the large aperture area of the PDs while generating a low BER amplified signal.

A. Choosing a Proper PD

PDs play a critical role in the design of VLC receivers. Hence, selecting appropriate PDs is one of the most important decisions in the design of such receivers. The active area of a PD is a critical factor. Large aggregate surface areas increase the FOV of the receiver but also reduce the effective bandwidth and increase the DC noise caused by background light. For mobile VLC, large FOV allows the receiver's performance to be more independent of the location of the transmitter. This, in turn, enhances the detection robustness of the receiver under mobility. Moreover, impingement of photons on the PD detection window generates a greater output current in PDs with larger active detection areas compared to those with smaller ones. PDs with large active areas reduce the need to employ high feedback resistance in transimpedance amplifier (TIA) circuits to convert data-carrying currents to voltage. Note that this reduction in resistance attenuates the thermal noise caused by the TIA circuit, further increasing the signal-to-noise ratio (SNR) at the amplifier output. On the other hand, increasing the active area of a PD increases its junction capacitor, consequently increasing its rise and fall times. This effect decreases the achievable bit rate and bandwidth of the PD, which in turn decreases the overall bandwidth of the receiver. Also, increasing the active detection area of the PD increases the low frequency (DC) dark current caused by background light at the PD output.

In our VLC receiver design, we used the PD FDS1010 by Thorlab [26] with a 1 cm^2 area. The large surface area of this PD is the first reason we decided to use it since other PDs in the market usually have 1 mm^2 active detection area. As another advantage, the considered PD also demonstrated the smallest rise time (highest bandwidth, ≈ 20 MHz) among all other PDs with the same active detection area of 1 cm^2 available in the market. Table II summarizes other relevant specifications of this PD.

In order to attain a 360° FOV, we organized an array of five FDS1010 PDs into a structure conformal to a cube as shown in Fig. 1(a) and wired them in parallel. The cubical structure of PD arrays allows omni-directional signal reception. Such PD arrays can be arranged in a way conformal to the surface of the mobile receiver unit, e.g., a laptop or smartphone. This cubic structure offers two main advantages: it considerably reduces the dependency of the signal quality on the corresponding spatial positions of the receiver and transmitter and, moreover, eliminates the need for employing optical components such as plano convex lenses, which are usually used for focusing the incident light on the small detection window of the PD in order to increase the output current generated by the incident light.

Although PD arrays could potentially increase the FOV to 360°, they also increase the delay spread of the channel impulse response, which in turn increases the ISI. Consequently, the average BER, particularly at high bit rates, also increases when deployed in a vibrant mobile VLC link. We will address these challenges in Sections VII and VIII.

B. Three-Stage Voltage Amplification

Amplifying the received signal with high gain while preserving stability plays an important role in providing a wide communication range for VLC links. Traditional amplification

TABLE II
Important characteristics of FDS1010

Specifications	
Wavelength Range, λ	$350 - 1100$nm
Peak Responsivity, $max[\mathcal{R}(\lambda)]$	0.725A/W
Active Area per PD, A	100mm^2
Rise/Fall Time, t_r/t_f ($V_B = 18V$)	18ns
Dark Current ($V_B = 18V$)	80μA
Capacitance, C_J ($V_B = 18V$)	169.2pF
Maximum Tolerable Reversed Biased, $V_{B,max}$	25V
Maximum Output Photocurrent, I_o	10mA
Maximum Optical Input Power, $P_{i,max}$	10mW

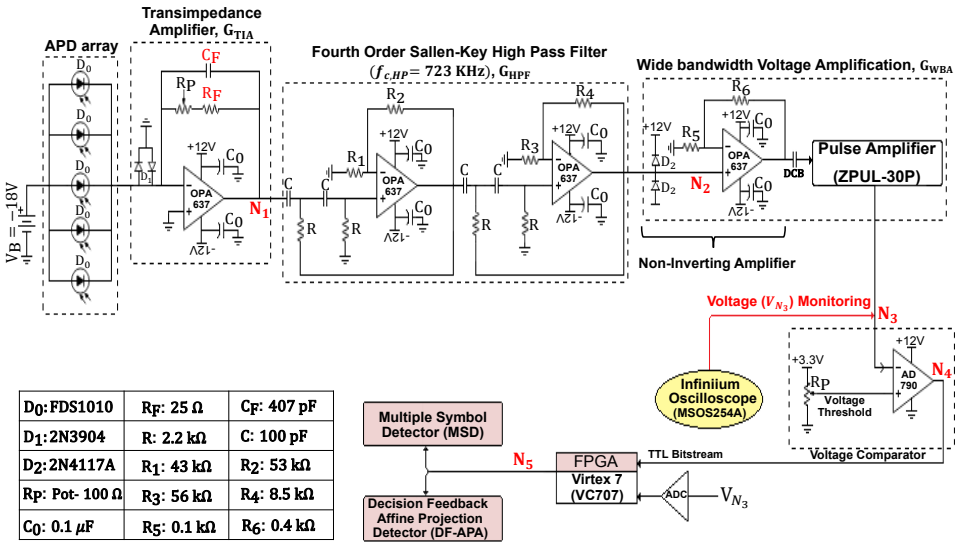

Fig. 3. VLC receiver circuit

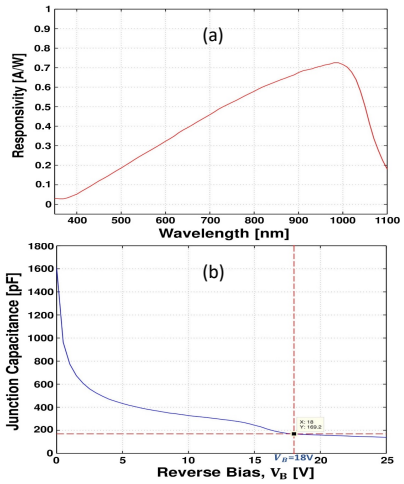

Fig. 4. Key specifications of the PD: (a) Responsivity; (b) Junction capacitance

of signals received from PD only involves the design of a single-stage trans-impedance amplifier (TIA), which can only be used for low-speed telecommunication and uses high feedback resistor $\mathrm{R_F}$ to attain high gain [17]. But, high $\mathrm{R_F}$ limits the bandwidth (as in Eq. (2)), and such designs are not appropriate for our VLC goals with large surface area PDs operating at high speeds. In order to maintain wide bandwidth, high gain and long communication range, we amplify and detect our data-carrying signal through three stages. The three stages include a transimpedance pre-amplification for current-to-voltage conversion (Stage 1) and a non-inverting amplifier for voltage amplification (Stage 2). Between these two stages we use a high pass Sallen-Key filter. As shown in Fig. 3, we further follow the wide bandwidth amplification of Stage 2 with a wideband pulse amplifier (Stage 3) which provides a 30 dB gain at a 500 MHz bandwidth. The overall gain of the receiver is:

$$\mathrm{G} = \frac{\mathrm{V_{out}}}{\mathrm{I_o}} = \mathrm{G_{TIA}G_{HPF}G_{WBA}} \tag{1}$$

where $\mathrm{V_{out}}$ is the output data-carrying analog voltage of the amplification, $\mathrm{V_{N_3}}$ in Fig. 3, and $\mathrm{I_o}$ denotes the output current generated by the PD arrays and is equal to $\int_{350\ \mathrm{nm}}^{1100\ \mathrm{nm}} N_{PD} P_i(\lambda)\mathcal{R}(\lambda)\ \mathrm{d}\lambda$ where $N_{PD} = 5$ is the total number of PDs used in the cubic array. P_i is the power spectrum of the incident light and $\mathcal{R}$ is the responsivity[1] of a single PD within a wavelength range of 350 to 1100 nm (Fig. 4(a)). Further, $\mathrm{G_{TIA}}$, $\mathrm{G_{HPF}}$, and $\mathrm{G_{WBA}}$ are the TIA gain (Stage 1), the gain of the high pass filter, and the gain of wideband amplification (Stages 2 and 3). Next, we will delve into finding the appropriate configurations of the high-pass filter as well as Stages 1 and 2 of the voltage amplification.

1) Biasing Circuit: A PD signal can be measured as voltage or current. The PD current measurement demonstrates far better linearity, offset, and bandwidth performance. The generated photo-current is proportional to the incident light power and it must be converted to a voltage using a transimpedance configuration. The PD can be operated with or without an applied reverse bias depending on the application-specific requirements. Application of a reverse bias (i.e., cathode positive and anode negative) can greatly improve the speed of response and linearity of the devices [27]. In our configuration, the detector is reverse biased to reduce PD's total junction capacitance, thus reducing its rise time, $\mathrm{t_r}$. Moreover, the reverse biasing technique was employed through active TIA in order to eliminate the dependency between the voltage of the PD's cathode pin and the feedback resistor, $\mathrm{R_F}$, responsible for converting voltage to current. As shown in Fig. 3, the cathode pin is connected to the inverting pin of the operational amplifier which has the same zero voltage as its non-inverting pin. As one of the advantages of this structure, the voltage difference between the two PD pins is independent of the undesirable variations of $\mathrm{R_F}$ caused by the changes in the ambient temperature. This, in turn, leads to further independence of the receiver bandwidth from the temperature conditions in indoor office environments.

The overall bandwidth (BW) of the receiver is directly determined by $\mathrm{R_F}$ as follows [28]:

$$\mathrm{BW}\ [Hz] = \sqrt{\frac{\mathrm{GBP}}{2\pi \times \mathrm{R_F} \times (\mathrm{C_J} + \mathrm{C_F})}} \tag{2}$$

where GBP is the gain bandwidth product of the operational amplifier (OPA637BP) and is equal to 80 MHz, $\mathrm{C_F}$ is the feedback phase-compensation capacitor, and $\mathrm{C_J}$ is the equivalent junction capacitance of the cubical structure which can be obtained by [29], [30]:

$$\mathrm{C_J} = \mathrm{A} \times \sqrt{\frac{\epsilon_0 \epsilon_r}{2\mu\rho(\mathrm{V_B} + \mathrm{V_{bi}})}} \tag{3}$$

where $\epsilon_0 = 8.854 \times 10^{-14}$ F/cm is the permittivity of the free space, $\epsilon_r = 11.9$ is the silicon dielectric constant, $\mu = 1,400$ $\mathrm{cm^2/(Volt * second)}$ is the mobility of the electrons at 300 K (average room temperature), ρ is the resistivity of the

[1]The responsivity of a PD is a measure of its sensitivity to light and is defined as the ratio of the output photocurrent to the incident light power at a given wavelength λ. In other words, it is a measure of the effectiveness of the conversion of light power into electrical current. Responsivity varies significantly and with the wavelength of the incident light, applied reverse bias, and temperature. It increases slightly by applying reverse bias due to improved charge collection efficiency in the PD.

silicon, V_{bi} is the built-in voltage of silicon, A=5 cm^2 is the overall active detection area of the cubical structure and V_B is the applied bias. The junction capacitance is directly used to determine the speed of the PD response, as in Eq. (2). Moreover, the PD's junction capacitance can be reduced by applying a higher reverse voltage (Fig. 4(b)) up to the 25 V, which is the maximum tolerable reverse bias for the PDs used in the cubic structure. The bias voltage reduces the junction capacitance, causing the PD to have a faster response (smaller rise and fall time). Applying a reverse bias, however, will increase the dark and noise currents.

Incorrect calculation of R_F and C_F leads to quick instability of the receiver and quick saturation of the operational amplifiers employed in the receiver. From the Barkhausen stability criterion [31], oscillation can occur if the phase margin is insufficient in the unit closed-loop gain of the TIA circuit [32]. Due to the inverting nature of the negative feedback, the phase shift in the feedback signal equals 180° at lower frequencies. When the signal's frequency increases (i.e., higher bit rates), the dominant pole of the operational amplifier will be able to increase the phase shift by 90°. Similarly, the pole introduced by the feedback network can increase the phase shift by another 90° leading to a 360° phase shift when the close loop gain equals 1. A phase shift of 360° causes self-sustaining oscillations. A phase shift close to 360° also causes heavy ringing in the output. Both cases (a phase shift equal or close to 360°) need phase compensation for stabilizing the TIA circuit.

Adding a bypass capacitor parallel to the feedback resistor not only provides the phase compensation required for ensuring phase margin, but also prevents gain peaking at high frequencies (close to 10 to 20 MHz) and protects the operational amplifier against saturation. It is, therefore, essential to calculate the required feedback capacitor to provide optimal compensation. However, as observed in Eq. (2), unfortunately the feedback capacitor C_F will limit the frequency response, eventually forcing us to make a trade off. As a result, our goal is to find the minimum value[2] for the compensation capacitor, C_F, needed to eliminate oscillation and minimize ringing. For this purpose we obtain the TIA's open loop gain and its feedback factor, respectively, as follows:

$$A_v(f) = \frac{a_0}{1 + j\frac{f}{f_c}} \tag{4}$$

$$\beta(f) = \frac{X_{C_J}}{R_F || X_{C_F} + X_{C_J}} = \frac{1 + j(2\pi f) R_F C_F}{1 + j(2\pi f) R_F (C_F + C_J)} \tag{5}$$

where f_c denotes the cut-off frequency of the OPA637 amplifier in the open-loop mode which is 90 Hz, $a_0 = 120$ dB represents the DC open loop gain of the amplifier. In addition, $X_{C_J} = \frac{1}{jC_J(2\pi f)}$ and $X_{C_F} = \frac{1}{jC_F(2\pi f)}$ are the impedance of the cubic PD and feedback capacitor corresponding to frequency, f, respectively. C_J represents the equivalent capacitance for the 5 parallel PDs (Eq. (3)), assuming a value of 846 pF at a bias voltage of V_B=18 V.

[2]Choosing unnecessarily large values for C_F for higher phase margin reduces our usable BW (i.e. Eq.(2)) and must be avoided in high speed VLC.

Finding the right value for the feedback capacitance C_F involves tuning its trade off with phase margin and bandwidth. Higher C_F means more stability (i.e., large phase margin) but less bandwidth. In this design, we target 45° of phase margin (i.e., 180° + $\angle A_v(f_i)\beta(f_i) = 45°$ where f_i is the intercept frequency which is obtained by solving $|A_v(f)\beta(f)| = 1$). The 45° phase margin provides a good compromise between stability and bandwidth, and enables us to obtain a closed-form C_F:

$$C_F = \frac{1 + \sqrt{1 + 4.8\pi \times R_F \times C_J \times GBP}}{2.4\pi \times R_F \times GBP}. \tag{6}$$

In order to make sure the biasing circuit does not become a bottleneck to the VLC receiver's BW, we need to select the feedback resistor R_F as large as possible (for high gain) while not limiting the maximum achievable BW of the PD FDS1010. To respect the BW of the PD, we must satisfy BW $[Hz] \geq f_{PD,3dB}$, where $f_{PD,3dB} \approx \frac{0.35}{t_r}$ is the frequency at which the PD output decreases by 3dB and is equal to 19.85 MHz when t_r is 18 ns measured at $V_B = 18$ V according to Table II. By substituting Eq. (6) in Eq. (2) and solving BW $[Hz] \geq 19.85$ $[MHz]$, we find the maximum value of R_F[3] as 25 Ω. Finally, by substituting $R_F = 25$ Ω in Eq. (6), C_F calculates to 407 pF.

2) Noise Management and DC Elimination: Using 5 parallel PDs at the input of the TIA circuit, the background light in office environments (which we measured in our lab to be around 400 Lux at a 2 m distance from the transmitter) along with dark current generates a DC voltage equal to $R_F \times (I_{dc} + I_{BG})$ (roughly 3 V in our lab) at the output of the TIA circuit. If this DC voltage is not effectively eliminated, saturation quickly occurs when amplifying the data carrying voltage, V_{N_1}. Moreover, this undesired DC voltage at the input of the non-inverting amplifier (N_2) limits the voltage swing at the output, V_{N_3}, which prevents us from high gain amplification of the data-carrying signal, consequently limiting the communication range accessible by the receiver. In order to eliminate the DC voltage from the output of the TIA stage and deduct the noise, we implement a fourth-order Butterworth Sallen-Key high pass filter [33], [34] with a cut-off frequency of 723 kHz ($\approx 0.7 \times R_{b,min}$). In order to obtain the appropriate values for the capacitors and resistors used in the filter, we write the transfer function of the filter as:

$$H_1(s) = \frac{V_{N_2}(s)}{V_{N_1}(s)} = \frac{(3 - k_1)(3 - k_2)}{(\frac{s^2}{\omega_c^2} + \frac{k_1 s}{\omega_c} + 1)(\frac{s^2}{\omega_c^2} + \frac{k_2 s}{\omega_c} + 1)} \tag{7}$$

where $\omega_c = 2\pi f_{c,HP} = \frac{1}{RC}$ and $f_{c,HP}$=723 kHz is the cut-off frequency considered for the high-pass filter and is obtained by setting R=2.2 kΩ and C=100 pF. Moreover, $k_1 = 2 - \frac{R_2}{R_1}$ and $k_2 = 2 - \frac{R_4}{R_3}$. Finally, by assuming $R_2 = 53$ $k\Omega$, $R_1 = 43$ $k\Omega$, $R_3 = 56$ $k\Omega$ and $R_4 = 8.5$ $k\Omega$, we find the desired values for $k_1 = 0.7654$ and $k_2 = 1.8478$, and the denominator in Eq. (7) becomes equivalent to $B_4(\frac{s}{\omega_c})$ where $B_4(s) = (s^2 + 0.7654s + 1)(s^2 + 1.8478s + 1)$ is a fourth-order Butterworth

[3]In order to take into account the capacitance and resistance caused by trace in the breadboard, the feedback resistor R_F is combined with a 100 Ω potentiometer in series and, if needed, the value of the feedback resistor is adjusted such that a stable state is achieved.

polynomial. As a result, a -80 dB decay (i.e., fourth-order decay) is experienced at the cut-off frequency of 723 kHz.

C. Symbol-by-Symbol Detection

Generation of a transistor-transistor logic (TTL)-compliant bitstream is among the very first and important steps in transmission and processing of the received signals using the FPGA digital processor. The amplified data-carrying voltage signal undergoes a two-level digitization for conversion to a TTL-compliant bitstream. The propagation delay of the comparator chip is a very important factor in maintaining the high bandwidth of the receiver system during the digitization of the data-carrier analog signals.

Offering a propagation delay of 45 ns, the AD790 is a great choice for transmission of information at bit rates in the order of 20 Mbps. Moreover, as another feature, the AD790 comparator chip offers the capability of adjusting the high-level voltage at the output bitstream. In order to maintain the output compatibility of the comparator and the general purpose input output (GPIO) of the FPGA processor, we set the high-level voltage to 3.3 V. The structure of the digitizer is shown in Fig. 3. In this structure, we use a 100 Ω potentiometer and a voltage source of 3.3 V to produce the threshold voltage. In our prototype, we determined the threshold voltage to be 0.8 V by averaging the sample data-carrier voltage signals at the output of the wideband amplifier during a 0.1 second period. After obtaining the TTL-compliant data-carrier bitstream[4] at the output of the comparator, the bitstream[5] is stored and received in a FPGA (Virtex 7) at its dual port RAM using the GPIO interface and displayed on a monitor.

IV. VLC Transmitter Design

The most important parameters when selecting the appropriate light source for VLC include maximum tolerable oscillation frequency [Hz], power usage level [W], brightness [Lux] and coverage area of the considered source. Phosphorus LEDs are the predominant choice for transmitters mostly because they can be switched on and off and oscillate in very short intervals (≈ 35-40 MHz) while providing a relatively high illuminance with a low power consumption [18]. As shown in Fig. 5(a), we consider four different structures (Types I-IV) composed of phosphorus LEDs for the transmitter. In the first structure, we focus on the effect of increasing the number of distributed LEDs on the brightness with a relatively high cross-sectional area in the absence of collimator lenses and, consequently, the maximum communication range. In the second and third structures, we studied the collimation of the ray emitted from the light source and its effects on the quality and communication range. In the fourth structure, we examine the phosphorus LEDs with a low divergence angle. The results of comparing these structures are in Table III.

[4]Our generated TTL bitstream is a single-ended signal, so that our voltage signal at the output of the digitizer consists of a voltage on one wire, referenced to a system ground and "low" and high voltage levels range from 0 to 0.2 V and 2 to 3.3 V, respectively.

[5]In order to reduce the errors in sampling of the received analog signal, the FPGA clock pulse frequency should be determined based on the data transmission rate, communication range, and careful consideration and observation of the eye diagram of the received signal at the comparator output.

Efficacy of light intensity generated by a light source is also a key parameter. To choose the appropriate light source, we measured the emission spectrums corresponding to the incident power of the four structures by using Thorlab's optical spectrum analyzer (OSA). Fig. 5(b) shows both absolute power [μW] and wavelength [nm] from our measurements at 1 m distance on the line-of-sight of the structures. As observed, we are having two major peaks, one around wavelength 445 nm (blue color) and the broad phosphorus spectrum centered near to 545 nm causing limitation in the overall achievable modulation bandwidth [35]. To reject the slow phosphorescent components, we placed a dichroic optical bandpass filter[6] in front of the PD arrays. This blue filter, by retaining only the blue light signals of the LED, improves the modulation bandwidth and BER of the VLC system by attaining high SNR [36]. Fig. 5(c) shows the output photo-current spectrum of the structures after their signals pass through the blue filter.

After comparing and examining the respective emission spectrums and luminous efficacy [Lux/W] for these four lighting candidates, we select the first structure for our VLC system prototype. Due to its relatively low electrical power consumption (36 W), this structure enables our receiver to generate the highest output current at the 1 m distance without the need for collimator lenses and heat management.

After selecting the appropriate light source, we design the transmitter system to send the data using an FPGA. To transmit the data-carrying bitstream through FPGA (Spartan 3E), the bitstream was stored at an internal single port ROM. The desired transmission bit rate can be adjusted up to 50 MHz by adjusting the pulse frequency of the clock.

The bits of the transmitted message enter the buffer circuit from the FPGA through the GPIO interface in an orderly manner and on the positive edge of the clock pulse, after which they appear at the buffer output. The reason to employ the buffer was to protect the FPGA processor pins against

TABLE III
Characteristic and efficiency measurements for different optical transmitters.

Parameter \ LED Model	Type (I)	Type (II)	Type (III)	Type (IV)
Number of LEDs Included in the structure	336	100	100	4
Diameter of the Collimator Lens [mm]	-	78	50	-
Focal Length of the Collimator Lens [mm]	-	50	44	-
Lambertian emission [Degree]	120	70	60	35
Illuminance at 1 meter distance [Lux]	7645	6246	5445	2100
Power Usage [W]	36.3	29.9	23.3	14.2
Luminous Efficacy [$\frac{\text{Lux}}{\text{W}}$]	210	208	233	147
Junction Capacitance [nF]	1.3	0.4	0.8	5.4
Max Communication Range (For Having BER$\leq 10^{-5}$ @ 1 Mbps) [m]	7.1	6	4.8	1.8
Heat Management Needed?	No	Yes	Yes	No
Lamp Base Shadow [Degree]	120	105	105	120

[6]Thorlabs FB450-40 Bandpass Filter, CWL = 450 ± 8 nm, FWHM = 40 ± 8 nm with 76% transmissivity (also demonstrated in Fig. 5(b) with green curve) at 445 nm.

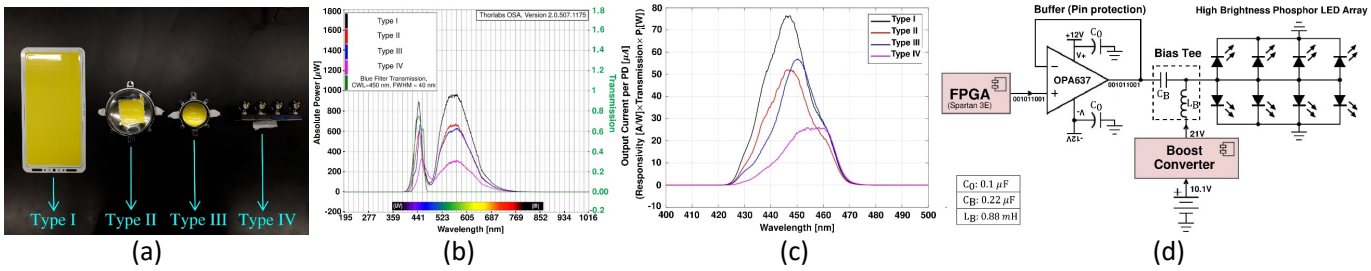

Fig. 5. (a) Light sources; (b) Emission spectrum; (c) Current spectrum; (d) Transmitter schematic

possible leakage of the DC current from DC branch to the signal-carrier branch. The operational amplifier OPA637 was used in the implementation of the considered buffer due to its high gain bandwidth product (≈ 80 MHz).

We used a wide-band bias tee to prevent the leakage of the data-carrier signal to the DC branch as well as to prevent the leakage of the DC current to the branch containing data signals. Fig. 5(d) demonstrates circuit of the transmitter. The DC branch in the transmitter circuit is responsible for supplying the appropriate DC voltage necessary for biasing the corresponding lighting structure employed in the transmitter. Furthermore, we utilized a boost converter in the DC branch in order to step up the biasing voltage (while stepping down the current) from its power supply to the output (which is connected to the LED panel). Battery power systems often stack cells in series to achieve higher voltage. However, sufficient stacking of cells is not a proper solution (or sometimes possible) in many high voltage applications due to lack of space. Boost converters can increase the voltage and reduce the number of cells. As a result, by using a single 9-Volt battery, we can provide the 18.1 V potential needed to drive and bias the LED panel.

V. VLC System Prototype and SISO Results

We implemented the VLC transmitter and receiver outlined in prior sections. Fig. 6 shows the prototype and experimental setup for the VLC system. To evaluate the performance of the designed receiver in the presence of vibration, the entire body of the receiver's structure was assembled and mounted on a servo motor. The Arduino microprocessor used for controlling the speed and motion direction of the servo motor allows development of an intense vibration pattern with our desired characteristics (i.e. frequency, acceleration, velocity, and displacement [37]) inserted on the designed receiver.

Various scenarios and sets of experiments were performed in this paper. In the first scenario, the eye diagram of the received signal at reception bit rates of 1 to 20 Mbps was plotted in the presence and absence of vibrations in the VLC system to evaluate the effect of vibration on the quality of received signals. The data for the eye diagram was obtained by superposition of the current digital signal in the comparator output ($\mathbf{N_4}$) for any individual bit on a single graph with amplitude versus time graph. The same operation was performed on a large number of the received symbols in the output signal (waveform), and the resulting graph indicated the average statistics of the signal, resembling an eye.

In a second scenario, we established real-time transmission and reception. To assess the average BER at bit rates from 1 to 20 Mbps in presence of vibration, we transmitted a 512×512 black and white image, and calculated the error probability by comparing the received and transmitted images. We repeated this procedure 1,500 times to obtain the average BER.

A. Inter-Symbol Interference

Real-time eye diagrams in Fig. 9 provide instant visual data that can be used to check the prototype's signal integrity in both absence (Fig. 9(c)(e)(g)) and presence of vibration (Fig. 9(d)(f)(h)). We also characterized and measured the vibration intensity of the considered indoor office setting, for both vibrant (Fig. 9(b)) and non-vibrant (Fig. 9(a)) VLC links.

As shown in Figs. 9(d)(f)(h) (from top to bottom), the increased ISI (which is due to the time varying receiver FOV caused by vibration in the receivers body) creates distortion and eye-closure. We also assessed the reception quality in the absence of vibration at different transmission bit rates by measuring the eye amplitude in Figs. 9(c)(e)(g). As shown, by increasing the transmission bit rate from 1 Mbps in Fig. 9(c) to a maximum 20 Mbps in Fig. 9(g), the respective eye amplitude is decreased, which is an indication of the decrease in the received SNR at the receiver output[7].

B. Maximum Speed and Range

To understand the VLC link's speed and range limits, we look at the performance of the VLC receiver at a bit rate of 20 Mbps in Fig. 9(g) and (h). The eye amplitude, in these cases, is approximately 100 mV (≥40 mV that is root mean square (RMS) noise voltage typical in room temperature), suggesting the capability of the VLC system in reception at a maximum transmission bit rate of 20 Mbps and communication range of 7 m when operating in both vibrant and non-vibrant VLC links. Any further increase in the bit rate leads to SNRs smaller than 1 at the receiver output, depriving the system of an effective reception and an acceptable BER.

We employ the suboptimal symbol-by-symbol detection (Section III-C) of the bitstream and plot the BER for different transmission bit rates from 1 to 20 Mbps at 7.1 m distance. Fig. 8 shows that average BER increases in the presence of vibration.

This behavior could also be predicted from the eye diagrams. Existence of vibration in the receiver body causes time variations in the FOV of the receiver, which in turn increases the delay spread in the impulse response of the channel (Fig. 7), ultimately generating and increasing the time-varying ISI.

[7]The receiver is able to detect and identify the transmitted bitstreams as long as the output voltage level is greater than the thermal noise voltage level (≈ 40mV-RMS).

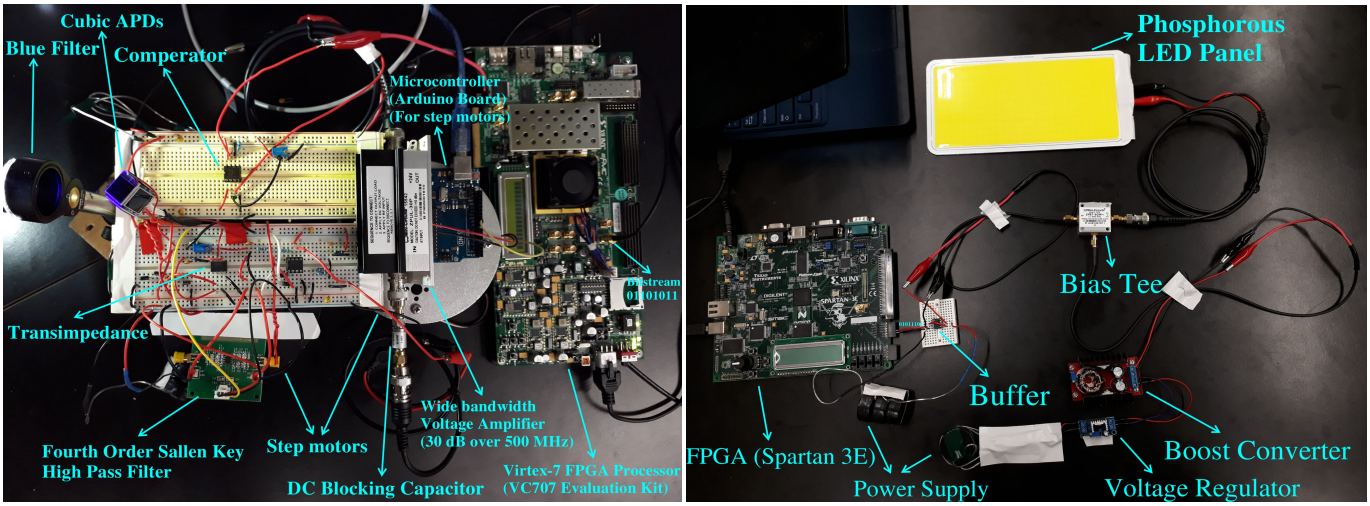

Fig. 6. VLC prototype: (a) Receiver; (b) Transmitter [1]

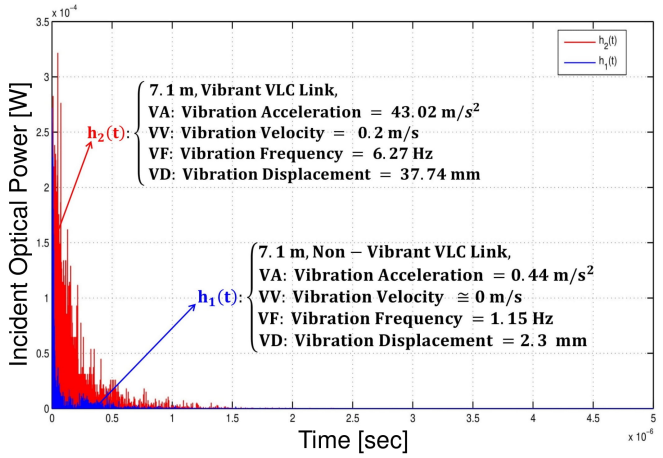

Fig. 7. Channel impulse response for vibrant and non-vibrant VLC links. [1]

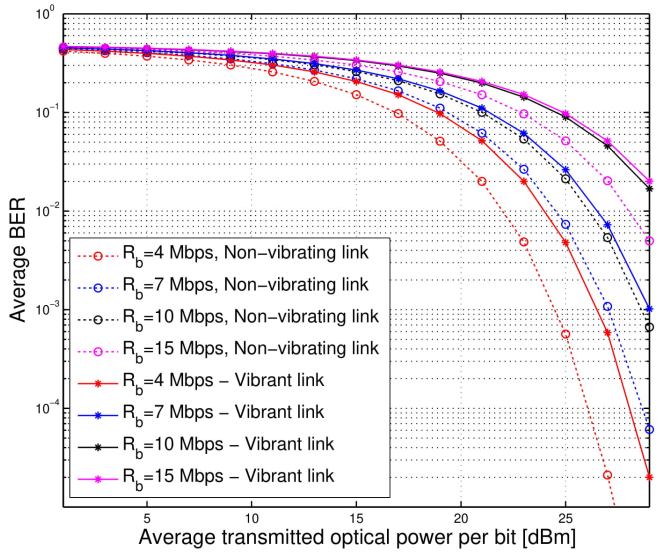

Fig. 8. BER performance results for vibrant and non-vibrant VLC links. [1]

This consequently increases and quickly saturates the average BER at bit rates close to 20 Mbps.

C. Channel Impulse Response

Understanding the effect of vibration on the VLC channel is crucial and, to the best of our knowledge, has not been empirically done before. From our prototype, we measure the channel impulse response to calculate the approximate delay spread of the VLC channel in both presence and absence of vibration (Fig. 7). High delay spread indicates the amount of ISI in the channel, and thus, tells a lot about the channel quality. To empirically measure the impulse response, we sent a 5μs high signal from the transmitter and stored $\mathrm{V_{N_2}}$ in a buffer. The stored $\mathrm{V_{N_2}}$ is proportional to the intensity of the incident light radiated on the PD. Finally, assuming linearity in the channel behavior [6], we estimated the channel impulse response by calculating the inverse FFT of the ratio of the FFT of $\mathrm{V_{N_2}}$ to the FFT of transmitted high signal of width 5μs. We also calculated the channel's RMS delay spread in both presence and absence of vibration using [6], [38], [39]:

$$\tau_{\mathrm{RMS},i} = \sqrt{\frac{\int_{-\infty}^{\infty}(t-\tau_i)^2 h_i^2(t)\mathrm{d}t}{\int_{-\infty}^{\infty} h_i^2(t)\mathrm{d}t}}, \quad i = 1, 2 \tag{8}$$

where τ_i is the mean delay due to non-LOS paths and is given by $\tau_i = \int_{-\infty}^{\infty} h_i^2(t)t\mathrm{d}t \Big/ \int_{-\infty}^{\infty} h_i^2(t)\mathrm{d}t$, i=1,2. Here, $\mathrm{h_2(t)}$ and $\mathrm{h_1(t)}$ are the estimated impulse responses for the VLC channel with or without vibration, respectively. By Eq. (8), we estimate the effective delay spread $\tau_{\mathrm{RMS},1}$=312.34 ns and $\tau_{\mathrm{RMS},2}$=7.04 ns over 7 m.

VI. SISO Link Performance Analysis

In this section, we use the Saddle-Point Approximation (SPA) [40], [41] to assess the BER performance of the prototype operating based on OOK modulation in vibrant and non-vibrant VLC links. The resulting analytical relations are then employed to study the system performance at different reception schemes. After a brief introduction of SPA, we then combine it with the statistical model for the receiver's output in Eq. (10) to obtain the analytical expression for calculation of system BER.

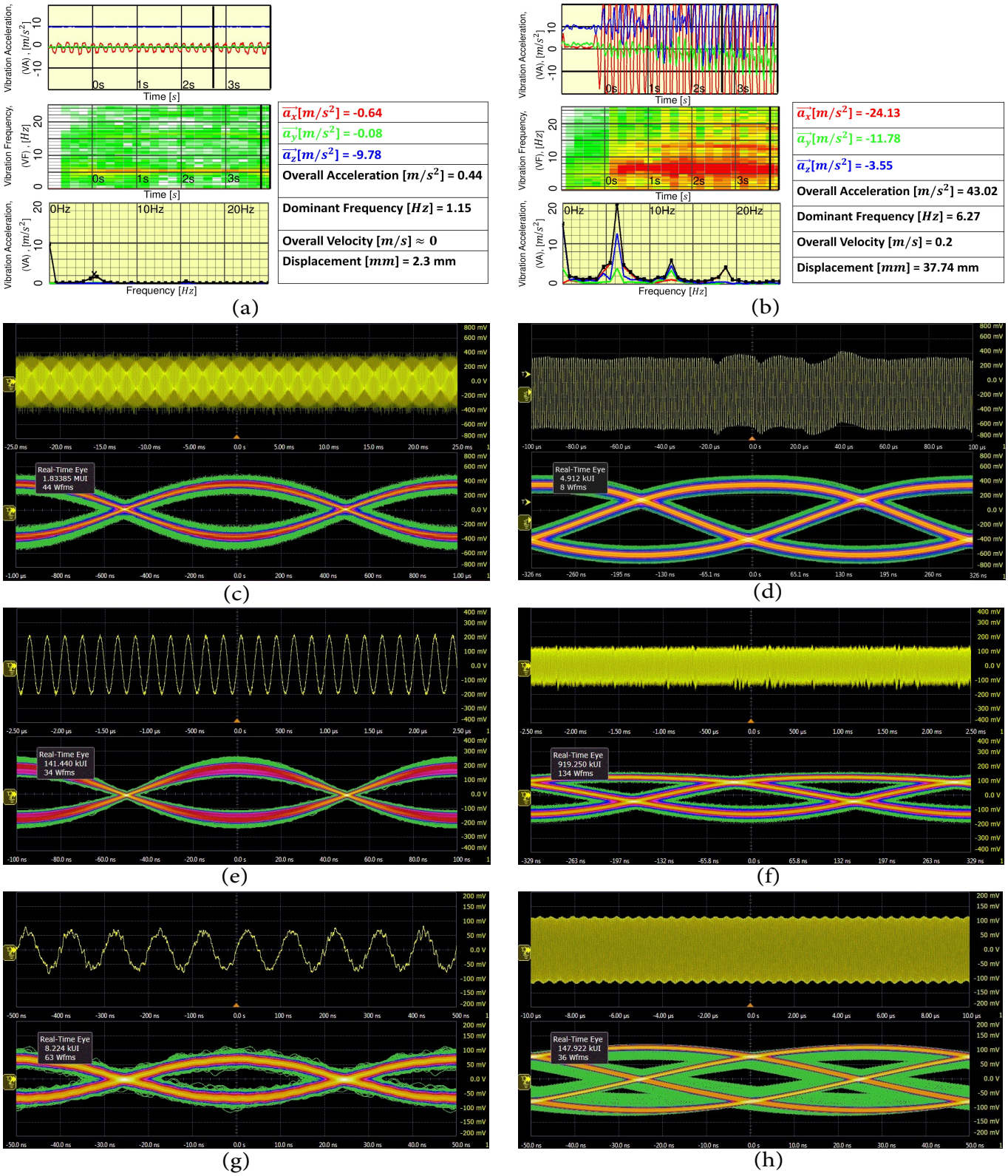

Fig. 9. Experimental results for both vibrant and non-vibrant, 7.1 m long VLC link: (a) Vibration conditions when communicating in a non-vibrant VLC link and (b) vibrant VLC link when step-motor (400 R.P.M.) operates, (c)(e)(g) from top to bottom: Eye diagrams for the 1, 10 and 20 Mbps data rates in a non-vibrant VLC link and (d)(f)(h) from top to bottom: vibrant (speed of 0.2 m/s, acceleration of 43.02 m/s^2, displacement of 37.74 mm, and frequency of 6.27 Hz) VLC-link.

A. System Model

On transmitter side, we have assumed intensity modulation direct-detection with On-Off Keying (OOK) modulation, i.e., 1s represented with high light intensity and 0s with low. As a result, the transmitted data sequence of the transmitter can be expressed as:

$$x(t) = \sum_{m=0}^{\infty} b_m P(t - kT_b) \tag{9}$$

where $T_b = \frac{1}{R_b}$ is the bit duration time and R_b is the data transmission rate. Moreover, in this scheme, bits “0” and “1”

of each time slot will be transmitted with pulse shapes 0 and $P(t)$, respectively, and $b_m \in [0,1]$ is the OOK modulated signal corresponding to the m^{th} transmitted bit (or symbol).

On the receiver side of the VLC system, the output data-carrying analog signal (i.e., V_{N_3} in Fig. 3) is integrated over consecutive bit times (i.e., $\int_{kT_b}^{(k+1)T_b} V_{N_3}(t)\mathrm{d}t$) and as a result a discrete signal is built in each time slot, i.e., $r(k)$ where k indicates the index of the time interval at which k^{th} transmitted bit is integrated. When a photon hits a PD, the generated output photo-current of the PD (i.e., the total number of generated photo-electrons) obeys a Poisson distribution [41]. The output of the integrator can be modeled as a Poisson Point Process whose average is in proportion with the total optical incident power [41]. The integrated output of the optical detector can be modeled as:

$$r(k) = y(k) + \nu_{b,d}(k) \tag{10}$$

where $\nu_{b,d}(k)$ is the Poisson noise (including background and dark current noises) during the detection of the k^{th} symbol in the receiver. $\nu_{b,d}(k)$ is a Poisson variable with an average value of $(n_b + n_d)T_b$, where $n_b = \frac{2\eta_Q \eta_E P_{BG} T_b}{hf}$ and $n_d = \frac{2I_{dc}BT_b}{q}$ are the number of photo-electrons generated by the background light and the dark current noise, respectively [6]. Here, η_Q represents the quantum efficiency of the PD [42]–[44], η_E is the elimination factor of the high-pass filter in our receiver, B is the overall electronic bandwidth provided by our prototype and was obtained in Eq. (2), P_{BG} is the received background power and I_{dc} is the dark current of PD hardware. $q = 1.602 \times 10^{-19} C$ is the elementary charge, $h = 6.626 \times 10^{-34}$ is Plank's constant, and f represents the frequency of the light source [41]. $y(k)$ is the count of photo-electrons generated from the received data-carrying signal, and is also a Poisson variable with an average in proportion to the PD output in the k^{th} interval. By considering the effects of the L detected symbols prior to detection of the k^{th} symbol on increasing the resulting average number of photo-electrons on the k^{th} interval, $y(k)$'s expected value will be:

$$m_y(k) = \frac{\tilde{\mathcal{R}}\tilde{h}}{q} \sum_{m=k-L}^{k} b_m \int_{(k-m)T_b}^{(k-m+1)T_b} \Gamma(t)\,\mathrm{d}t \tag{11}$$

where $\tilde{\mathcal{R}}$ is the responsivity of the cubical PD at the corresponding wavelength of the incident light ($\lambda = 445$ nm, Blue color)[8], and $\tilde{h}$ is a positive multiplicative fading coefficient (to characterize turbulence effects). Further, $\Gamma(t) = h(t) * P(t)$ where $h(t)$ is the impulse response of the vibrant VLC channel (which we empirically estimated in Fig. 7) and L is the channel memory which increases with the vibration intensity, data rate, transmitter beam divergence angle, receiver FOV, and distance. Eqs. (10) and (11) imply that $r(k)$ is a Poisson variable with an average $m(k)$ defined by

$$m(k) = \tilde{m}(k)\tilde{h} + (n_b + n_d)T_b \tag{12}$$

[8] $\tilde{\mathcal{R}}$, the responsivity of our cubic PD structure, can be obtained as $N_{PD} \times G \times \mathcal{R}|_{\lambda=445\text{nm}}$ where $N_{PD} = 5$ is the total number of PDs used in the cubic structure, G is the overall receiver gain in Eq. (1), and $\mathcal{R}$ is the responsivity of one PD (Fig. 4(a)).

where $\tilde{m}(k)$ is defined according to

$$\tilde{m}(k) = \frac{\tilde{\mathcal{R}}}{q} \sum_{m=k-L}^{k} b_m \int_{kT_b}^{(k+1)T_b} \Gamma(t - mT_b)\,\mathrm{d}t. \tag{13}$$

For the first time in this study, the effect of interfering bits caused by the delay spread present in the channel impulse response is modeled by the relation obtained for $m_y(k)$ in Eqs. (12) and (13). This in turn allows a highly accurate assessment of the receiver performance in VLC links, specifically the vibrant types which cause a significant delay spread for the propagated photons and intensify the interference of transmitted photons in bits preceding the k^{th} bit during the decision-making process for this bit. Using SPA [40], [41], the system BER can be obtained as $BER = \frac{1}{2}\left[q_+(\nu_{th}) + q_-(\nu_{th})\right]$, where $q_+(\nu_{th})$ and $q_-(\nu_{th})$ are probabilities of error when bits 0 and 1 are sent. We can write $q_+(\nu_{th})$ and $q_-(\nu_{th})$ as

$$\begin{aligned}
q_+(\nu_{th}) &\triangleq \Pr(U > \nu_{th}|zero) \approx \frac{\exp\left[\Psi_0(s_0)\right]}{\sqrt{2\pi\Psi_0''(s_0)}} \\
q_-(\nu_{th}) &\triangleq \Pr(U \leq \nu_{th}|one) \approx \frac{\exp\left[\Psi_1(s_1)\right]}{\sqrt{2\pi\Psi_1''(s_1)}} \\
\Psi_0(s) &\triangleq \ln\left[\phi_{U,0}(s)\right] - s\nu_{th} - \ln|s| \\
\Psi_1(s) &\triangleq \ln\left[\phi_{U,1}(s)\right] - s\nu_{th} - \ln|s|
\end{aligned} \tag{14}$$

where $U = r(0)$ is the received detector output during interval of [0, T_b] and is obtained according to Eq. (10). Furthermore, s_0 is the positive and real root of $\Psi_0'(s)$, i.e., $\frac{\mathrm{d}\Psi_0(s)}{\mathrm{d}s}|_{s=s_0} = 0$ and s_1 is the negative and real root of $\Psi_1'(s)$, i.e., $\frac{\mathrm{d}\Psi_1(s)}{\mathrm{d}s}|_{s=s_1} = 0$. ν_{th} is the optimum voltage threshold used in the receiver for optimum detection and can be optimally calculated to minimize the BER, i.e., $\frac{\mathrm{d}BER}{\mathrm{d}\nu_{th}} = 0$. $\phi_{U,0}(s)$ and $\phi_{U,1}(s)$ are moment generating functions (MGF) of the receiver output's amplified photo voltage (U) when bits "0" and "1" are transmitted, respectively and can be obtained according Eqs. (15)-(18)

$$\phi_U(s) = \frac{1}{2^L} \sum_{b_{-1},..,b_{-L}} \int_0^\infty \phi_{U|(b_{-1},..,b_{-L},\tilde{H}=\tilde{h})}(s) f_{\tilde{H}}(\tilde{h})\mathrm{d}\tilde{h} \tag{15}$$

$$\begin{aligned}
\phi_{U|(b_{-1},..,b_{-L},\tilde{H}=\tilde{h})}(s) &= E\left\{e^{sU}|(b_{-1},..,b_{-L},\tilde{H}=\tilde{h})\right\} \\
&= \exp\left[(m_y(0) + (n_b + n_d)T_b)\left(\exp(s) - 1\right)\right]
\end{aligned} \tag{16}$$

$$\phi_{U,0}(s) \triangleq \phi_U(s)|_{\text{Bit 0 is sent i.e., } (b_k=0|_{k=0})} \tag{17}$$

$$\phi_{U,1}(s) \triangleq \phi_U(s)|_{\text{Bit 1 is sent i.e., } (b_k=1|_{k=0})} \tag{18}$$

where L represents the channel memory and $\tilde{h}$ is a random variable with Erlang distribution

$$f(\tilde{h}; \lambda_F, \theta_F) = \frac{\lambda_F^{\theta_F}}{(\theta_F - 1)!}\tilde{h}^{\theta_F - 1} e^{-\lambda_F \tilde{h}}, \quad \tilde{h} \geq 0. \tag{19}$$

In Eq. (19), $\lambda_F \in \mathbb{R}$ and $\theta_F \in \mathbb{Z}^+$ are selected so that the Erlang function conforms to the normalized Lognormal function with a variance of $\sigma_{\tilde{h}}^2$ and mean value 1 [45], [46] which is the typical case in VLC indoor links.

and as a result the BER can be numerically computed as

$$BER = \frac{1}{2}(q_+(\nu_{th}) + q_-(\nu_{th})) = \\ = \frac{1}{2}\left[\frac{\exp\left[\Psi_0(s_0)\right]}{\sqrt{2\pi\Psi_0''(s_0)}} + \frac{\exp\left[\Psi_1(s_1)\right]}{\sqrt{2\pi\Psi_1''(s_1)}}\right] \quad (20)$$

Appendix A details how the expression in Eq. (20) is calculated. However, to calculate the BER above, the roots for s_0, s_1, ν_{th} are necessary. To obtain these roots, we utilize the Quasi-Newton Method by solving the following system of nonlinear equations for s_0, s_1, $\nu_{th} \in \mathbb{R}$:

1) $\frac{\mathrm{d}\Psi_0(s)}{\mathrm{d}s}|_{s=s_0} = 0$
2) $\frac{\mathrm{d}\Psi_1(s)}{\mathrm{d}s}|_{s=s_1} = 0$
3) $\frac{\mathrm{d}BER}{\mathrm{d}\nu_{th}} = 0.$

We, then, use the solutions for s_0, s_1 and I_{th} for calculating the most accurate approximation of BER.

VII. Multiple-Symbol Detection

Drawing on the experimental results, we obtained the impulse response of the VLC channel in the previous section (Fig. 7), revealing that the delay spread of the channel drastically increases in the presence of the intense vibration in the receiver. The delay spread interrupts the symbols transmitted on the channel and deteriorates the overall performance of the optical system, which in turn limits the communication range. In this section, we design an optimal detector, aiming to restore the performance lost in symbol-by-symbol detection due to the ISI in which detection decisions are made using a multi-bit observation window.

To achieve an optimal decision metric for VLC receiver, we obtain the joint probability distribution function of the $r(0)$, $r(1)$, …, $r(N-1)$ as[9]

$$M_{MSD}(\underline{b}) = \frac{1}{2^L} \times \prod_{i=0}^{N-1} \sum_{b_{i-1},..,b_{i-L}} \\ \left[\int_0^\infty Poiss(\ r(i)|\ b_i, (b_{i-1},..,b_{i-L}), \tilde{h}_i) f(\tilde{h}_i)\, \mathrm{d}\tilde{h}_i\right], \quad (21)$$

where N is our desired window length. By substituting Eq. (19) in Eq. (21), we obtain our optimum decision metric as

$$M_{MSD}(\underline{b}) = \frac{1}{2^L} \times \frac{((n_b+n_d)T_b)^{r(i)}}{r(i)!} \times \frac{\lambda_F^{\theta_F} e^{-(n_b+n_d)T_b}}{(\theta_F-1)!} \\ \times \prod_{i=0}^{N-1} \sum_{b_{i-1},..,b_{i-L}} \frac{e^{\mu\nu} g_{\theta_F-1}(r(i);\mu(i),\nu(i))}{\nu(i)(\mu(i)\nu(i))^{r(i)}} \quad (22)$$

where $g_\theta(a;b,c) = c^{a+1}\int_0^\infty x^\theta (x+b)^a e^{-c(x+b)}\mathrm{d}x$, $\nu(i) = \tilde{m}(i) + \lambda_F$ and $\mu(i) = \frac{(n_b+n_d)T_b}{\tilde{m}(i)}$. Since only the last term in Eq. (22) includes the detected bits b_is, the receiver needs to consider only that term for optimal decision on what bits were transmitted. Thus, the optimal receiver must select a bit vector from the 2^N possible bit vectors $\hat{\underline{b}} = [b_0, b_1, \ldots, b_{N-1}]$. It will do so by solving the following maximization problem:

$$\hat{\underline{b}}_{N\times 1} = \underset{\underline{b}}{\operatorname{argmax}} \prod_{i=0}^{N-1} \sum_{b_{i-1},..,b_{i-L}} \frac{e^{\mu(i)\nu(i)} g_{\theta_F-1}(r(i);\mu(i),\nu(i))}{\nu(i)(\mu(i)\nu(i))^{r(i)}} \quad (23)$$

In Section X, we exhaustively search all possible bit vectors which incurs a computational complexity of $O(2^N)$. Next, we design a prediction algorithm to relieve this complexity.

[9]The sum symbol $\sum_{b_{i-1},b_{i-2},\ldots,b_{i-L}}$ is used to define the summation over all possible binary sequences for $b_{i-1}, b_{i-2}, \ldots, b_{i-L}$. The division of the resulting sum by $\frac{1}{2^L}$ leads to the average value over all possible bit combinations.

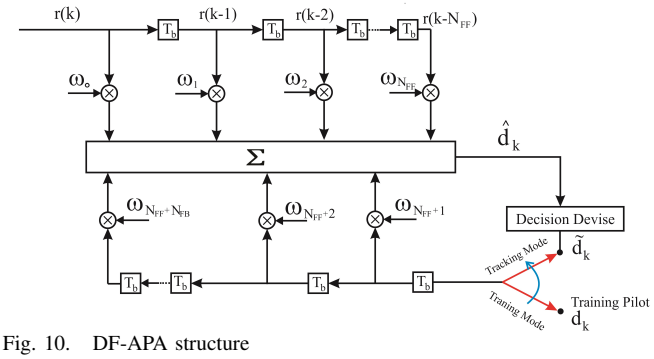

Fig. 10. DF-APA structure

VIII. Adaptive Symbol Detection

As VLC industry moves to data rates of 10 Mbps and beyond, ISI becomes a more significant problem compared to the lower data rates used previously. As it was concluded from the experimental results obtained from the prototype, ISI can result in complete eye closure at bit rates close to 20 Mbps in presence of vibration. Moreover, the vibration in the receiver's structure causes the FOV of the system to vary with time, which itself causes time-varying ISI. Furthermore, factors such as temperature and bending also exacerbate this problem. The time-varying nature of ISI means that effective solutions need to constantly adapt to the changing channel characteristics. In the previous section, we considered an approach using exhaustive search. In this section, we design and analyze a two-mode operational adaptive detector, namely, "Decision Feedback - Affine Projection Algorithm" (DF-APA) to take advantage of its adaptive and time-diverse reception capability and tackle the ISI problem. This approach lends itself well to mixed-signal designs that can attain similar performance to the optimum MSD techniques. Moreover, the adaptive detector discussed in this section offers a considerably lower computational complexity with a polynomial order.

A. System Model

The main idea behind decision feedback detectors is that when the data symbol is detected and decided, one can obtain and eliminate ISI on the future symbols prior to detection of the next symbols [47], [48]. This algorithm can be constructed as a feed forward (FF) filter and feedback (FB) filter in the optical receiver. ISI created by previously detected symbols on the current symbol can be adjusted using FB filter coefficients. Detector consists of N_{FF} + 1 taps in its FF filter and N_{FB} taps in its FB filter. As shown in Fig. 10, the adaptive system works in two modes, i.e, training and tracking modes, to detect the

transmitted symbols. When in the training mode, the detector's output will be

$$\hat{d}_k = \sum_{n=0}^{N_{FF}} [\omega_n r(k-n)] + \sum_{i=1}^{N_{FB}} [\omega_{N_{FF}+i} d_{k-i}] = \underline{\omega}^T(k)\underline{u}(k) \tag{24}$$

where $\underline{u}(k) = [r(k) \ \dots \ r(k-N_{FF}) \ d_{k-1} \ \dots \ d_{k-N_{FB}}]^T$ is the input signal of the detector seen in Fig. 10, $\omega_{i=0,\dots,N_{FF}+N_{FB}}$ are the gain coefficients (taps) used in the detector, $\underline{\omega}(k) = [\omega_0 \ \omega_1 \ \omega_2 \ \dots \ \omega_{(N_{FF}+N_{FB})}]^T$ represents the impulse response of the overall discrete adaptive filter containing both FF and FB tap weight coefficients after being updated for k times, and d_i is the input training sequence. Based on the conventional protocol between the transmitter and receiver, the training sequence bits d_i can be made available in the transmitted preamble packets, allowing the receiver to have full knowledge of these preamble bits and have full access to the training sequence. By obtaining the detector's output $\hat{d}_k$ in Eq. (24), the error signal e_k is determined using $d_k - \hat{d}_k$ and $\tilde{d}_k - \hat{d}_k$ in the training and tracking modes, respectively. Here, $\tilde{d}_k$ can be computed as

$$\tilde{d}_k = \begin{cases} 1 & \hat{d}_k \geq \mathrm{V_{Th}} \\ 0 & \hat{d}_k < \mathrm{V_{Th}} \end{cases} \tag{25}$$

where $\mathrm{V_{th}}$ is the voltage threshold and is the average output voltage over multiple symbols. This method eliminates the need for channel state information in the receiver for generating the training sequence in tracking mode. The error signal is squared to obtain the mean square error at the instant of k, leading to

$$J(k) = E\{|e_k|^2\} \tag{26}$$

where $J(k)$ is the cost function at the instant of k.

Adaptive symbol detectors need a specific algorithm for updating adaptive filter coefficients in the detector to minimize the desired cost function. There is a variety of adaptive algorithms for updating filter coefficients. In this case, we used the Affine Projection Algorithm (APA) [49] for iteration by iteration update of tap weight vector coefficients $\underline{\omega}(k)$ in Eq. (24). APA is the generalized form of the well-known NLMS adaptive algorithm in which each tap weight vector update can be considered as a one-dimensional affine projection. In APA, projections are made in multiple dimensions. Despite an increase in the convergence speed with increasing the number of projection dimensions, computational complexity of the algorithm unfortunately also increases [50], [51]. Here, we have utilized a two dimensional APA algorithm which enables us to minimize the mean square error (MSE) between the output $\hat{d}_k$ and training sequence d_k, while converging to the optimum tap weight vector coefficients faster than the general NLMS algorithms. In the following subsection, the proposed algorithm is described in detail.

B. Configuring the Adaptive Filter

Given the set of tap-input vectors $\underline{u}(k)$, $\underline{u}(k-1)$, $\dots$ $\underline{u}(k-(N_{FF}+N_{FB})+1)$ and the set of desired output samples d_k, $d_{k-1} \ \dots \ d_{k-(N_{FF}+N_{FB})+1}$, the tap-weight vector $\underline{\omega}(k+1)$ will be updated so as to minimize the squared Euclidean norm of the difference $\underline{\omega}(k+1)$-$\underline{\omega}(k)$ subject to $\underline{\omega}^T(n+1)\underline{u}(n-i) = d_{n-i}$ for $i = 0, \ 1, \dots \ M-1$ as a sets of constraints. Here, M is the number of applied constraints (i.e., dimensions). By increasing M, the convergence speed increases. However, this increase is limited by a threshold, after which its effect is negligible and further increment of M adds to the computational complexity. Note that NLMS algorithm is a special case of APA for M=1. In our DF-APA design, both in training and tracking modes, we set M=2 to increase the convergence speed compared to the common NLMS algorithm while maintaining the computational complexity at a moderate level. To update the tap weight vector in DF-APA, we formulate the following recursive optimization problem:

$$\min \quad \|\underline{\omega}(n+1) - \underline{\omega}(n)\|^2 \tag{27}$$
$$S.t. \begin{cases} \underline{\omega}^T(n+1)\underline{u}(n) = d_n \\ \underline{\omega}^T(n+1)\underline{u}(n-1) = d_{n-1}. \end{cases}$$

This optimization problem can best be solved using Lagrange multipliers [52], for which a recursive solution equation can be written as

$$\underline{\omega}(n+1) = [\mathrm{I} - \mu \mathrm{A}^T(n)[\mathrm{A}(n)\mathrm{A}^T(n)]^{-1}\mathrm{A}(n)]\underline{\omega}(n) + \mu \mathrm{A}^T(n)[\mathrm{A}(n)\mathrm{A}^T(n)]^{-1}\underline{d}(n) \tag{28}$$

where μ is the step size for controlling the algorithm's overall stability and convergence speed, $\mathrm{A}^T(n) = [\underline{u}(n), \ \underline{u}(n-1), \ \dots, \ \underline{u}(n-M+1)]$ and $\underline{d}^T(n) = [d_n, \ d_{n-1}, \ \dots, \ d_{n-M}]$ and M=2. The computational cost of solving Eq. (22) is $O(M(N_{FF}+N_{FB}))$ per sample (iteration) [51], [53].

TABLE IV
COMPLEXITY OF SYMBOL DETECTION.

Algorithm	DF-APA	MSD	SBSD
Memory	$O(N_{FF}+N_{FB})$	$O(N)$	$O(1)$
Computation	$O(M(N_{FF}+N_{FB}))$	$O(2^N)$	$O(1)$

IX. SPATIAL DIVERSITY COMBINING SIMO RECEIVERS FOR VIBRANT VLC LINKS

In this section we aim to increase the robustness of VLC receivers against vibrations in their physical structures. We design an Optimum Gain Combining (OGC) method for our SIMO VLC system as a solution to increase availability of

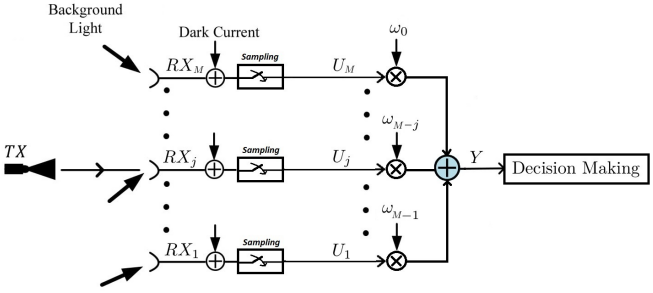

Fig. 11. SIMO VLC receiver with gain combination

the PD array under vibration without sacrificing the maximum available bandwidth of the receiver. Optimum here refers to the fact that instead of the common sub-optimum Equal Gain Combination (EGC) method, OGC optimizes the detection by maximizing the receiver output's SNR in the SIMO structure. Note that this structure allows the designer to install multiple independent PDs at different locations on, for example, smartphones, and take advantage of spatial diversity more effectively. We then outline the analytical relations between the received SNR and the number of employed receiver PDs. Additionally, we discuss the OGC detection method in detail and show how this method can automatically adapt to the link conditions without any user intervention to optimally combine the received symbols maximizing the receiver performance. Also, we use the SPA method again to assess the BER performance of the SIMO-OGC system and demonstrate its superiority compared to single PD structures accumulating a large aperture area.

As mentioned earlier, a PD with large active detection area can be employed as a suitable solution to increase the availability of VLC links and reduce the dependency of their performance on the sudden spatial dispositions of the receiver. However, As expressed in Eq. (2), despite increasing receiver robustness against casual user dispositions, employing PDs with a larger aperture area or paralleled PDs can, on the other hand, increase the effective junction capacitance (i.e., $\mathrm{C_J}$) of the PD structure, intrinsically limiting the maximum available bandwidth of the receiver. In addition, such a high aperture area increases the time delay spread present in the channel impulse response, specifically in vibrant VLC links. This is due to the fact that a higher aperture area means the receiver is more likely to detect photons scattered by multiple reflections and having a higher time delay compared to line-of-sight photons. As a result, the photons corresponding to the i^{th} bit are more likely to interfere with those corresponding to the $(i+1)^{\text{th}}$ bit, consequently increasing the ISI and further reducing the SNR of the received signal in the i^{th} interval.

A. Spatial Diversity: SIMO VLC Receivers

The proposed structure for SIMO receivers is presented in Fig. 11. As shown, the data-carrier signal is received through M independent reception links each having a PD with an identical active detection area equal to A/M. Each received signal in the i^{th} link is amplified by an allocated tap gain (i.e., ω_i). Ultimately, the decision-making process is carried out based on the weighted sum of all received signals from all receiver links. In what follows, the procedure for selection of the optimal gain vector to increase SNR and BER performance is discussed and the relationship between the number of links and detection performance of the system is studied in detail. The output of the proposed structure is as follows:

$$Y_{1\times 1} = \sum_{i=0}^{M-1} \omega_i U_{M-i} = \underline{\omega}^T \underline{U} \tag{29}$$

where Y is the output signal obtained based on the weighted sum of all received signals in all receiver links, $\underline{\omega} = [\omega_0 \ \omega_1 \ \omega_2 \ \dots \ \omega_{(M-1)}]^T$ represents the gain vector, ω_i is the gain corresponding to the i^{th} link, $U_i(k) = r_i(k)$ is the received output signal within the k^{th} time interval from the i^{th} link with Poisson distribution with mean $m_{y_i}(0)+(n_b+n_d)T_b$, $m_{y_i}(0)$ is obtained by substituting the corresponding channel impulse response for the i^{th} link (i.e., $h_i(t)$) in to the Eq. (11), and $\underline{U} = [r_M(0) \ \dots \ r_1(0)]^T$ is the input signal of the detector seen in Fig. 11. The output power of the receiver is then obtained as follows:

$$P_o = E\{|Y|^2\} = \underline{\omega}^T E\{\underline{U}\underline{U}^T\}\underline{\omega} = \underline{\omega}^T \ R_U \ \underline{\omega} \tag{30}$$

where $R_U = E\{\underline{U}\underline{U}^T\}$ denotes the autocorrelation matrix corresponding to the receiver's output. By utilizing the output power expression in Eq. (30), the output SNR of the SIMO structure with M independent receivers is:

$$\mathrm{SNR} = \frac{P_s}{P_N} = \frac{\underline{\omega}^H \ R_s \ \underline{\omega}}{\underline{\omega}^H \ R_n \ \underline{\omega}} \tag{31}$$

where R_s and R_n denote the autocorrelation matrices corresponding to the receiver's output in the absence of external noise (data signal only) and data-carrier signal (noise only), respectively. The following relations are obtained for R_s and R_n:

$$R_s = \begin{bmatrix} \sigma_{S_M}^2 + \sigma_{S_M}^4 & (\sigma_{S_M}\sigma_{S_{M-1}})^2 & \dots & (\sigma_{S_M}\sigma_{S_1})^2 \\ (\sigma_{S_M}\sigma_{S_{M-1}})^2 & \sigma_{S_{M-1}}^2 + \sigma_{S_{M-1}}^4 & \dots & (\sigma_{S_{M-1}}\sigma_{S_1})^2 \\ \vdots & \vdots & \ddots & \vdots \\ (\sigma_{S_M}\sigma_{S_1})^2 & (\sigma_{S_{M-1}}\sigma_{S_1})^2 & \dots & \sigma_{S_1}^2 + \sigma_{S_1}^4 \end{bmatrix} \tag{32}$$

$$R_n = \begin{bmatrix} \sigma_{N_M}^2 + \sigma_{N_M}^4 & (\sigma_{N_M}\sigma_{N_{M-1}})^2 & \dots & (\sigma_{N_M}\sigma_{N_1})^2 \\ (\sigma_{N_M}\sigma_{N_{M-1}})^2 & \sigma_{N_{M-1}}^2 + \sigma_{N_{M-1}}^4 & \dots & (\sigma_{N_{M-1}}\sigma_{N_1})^2 \\ \vdots & \vdots & \ddots & \vdots \\ (\sigma_{N_M}\sigma_{N_1})^2 & (\sigma_{N_{M-1}}\sigma_{N_1})^2 & \dots & \sigma_{N_1}^2 + \sigma_{N_1}^4 \end{bmatrix} \tag{33}$$

where $\sigma_N^2 = (n_{b_i} + n_{d_i})T_b$ is the noise component's variance at i^{th} link, n_{b_i} is the background noise and is obtained by considering P_{BG_i} as the background light power at i^{th} link and $\sigma_{S_i}^2$ i=1,..., M is the data signal's variance obtained as

$$\sigma_{S_i}^2 = \frac{1}{2^L} \sum_{b_0,..,b_{-L}} \int_0^\infty (m_{y_i}(0) + m_{y_i}^2(0)) f(\tilde{h}) \, \mathrm{d}\tilde{h}. \tag{34}$$

In order to obtain the optimal gain vector maximizing the output SNR, Eq. (31) can be differentiated with respect to $\underline{\omega}$ as follows:

$$\underline{\omega}_{opt} = \arg\max_{\underline{\omega}} \ (\mathrm{SNR}) \Rightarrow \underline{\omega}_{opt} = \arg\max_{\underline{\omega}} \ \left[\frac{\underline{\omega}^H \ R_s \ \underline{\omega}}{\underline{\omega}^H \ R_n \ \underline{\omega}}\right]$$
$$\xrightarrow{\frac{\partial \mathrm{SNR}}{\partial \underline{\omega}}} \underline{\omega}_{opt} : \ \left[\underline{\omega}_{opt}^T \ R_n \ \underline{\omega}_{opt}\right] R_s = \left[\underline{\omega}_{opt}^T \ R_s \ \underline{\omega}_{opt}\right] R_n \tag{35}$$

B. Special Case: Suboptimal Equal Gain Combination (EGC)

The conventional, suboptimal EGC method is investigated and evaluated in this subsection. Additionally, the conditions under which this method can offer close performance as the optimal OGC method are discussed. Given that in EGC algorithm, the decision variable Y is simply composed of unweighted sum of variables U_1 to U_M, the hardware implementation of the EGC method is easier, due to which this

suboptimal method is extensively employed in different studies. In this subsection, for the first time, we analytically show that under which specific conditions and assumptions for the VLC link, the OGC detection method obtained in the previous subsection is transformed into the EGC method. Subsequently, in order to characterize the relationship between SNR and the number of reception branches utilized in the SIMO structure, we obtain a closed-form analytical expression for the SNR of suboptimal SIMO-EGC. This analytical expression can be used as a lower limit for the SNRs achievable using the SIMO-OGC structures. Furthermore, it provides the designer with the elbow-room to select the appropriate number of branches in the SIMO structure so as to strike a balance between the final production cost of the receiver and its SNR, reception quality and communication range.

The relation obtained for R_n in Eq. (33) can be approximated as follows by assuming equal external noise in all M links and neglecting the non-diagonal elements of R_n:

$$R_n \approx (\sigma_N^2 + M\sigma_N^4) I_M \tag{36}$$

where $\sigma_N^2 = (n_b + n_d)T_b$ and I_M is an M by M unitary matrix. It can also be shown that under above mentioned assumptions the corresponding approximation leads to eigenvalues identical to the exact R_n. Furthermore, If we assume all corresponding channel impulse responses to be equal for all links (i.e., $h_1(t) = h_2(t) = ... = h_M(t)$) the R_s expression in Eq. (32) is simplified to

$$R_s = \begin{bmatrix} \sigma_S^2 + \sigma_S^4 & \sigma_S^4 & \dots & \sigma_S^4 \\ \sigma_S^4 & \sigma_S^2 + \sigma_S^4 & \dots & \sigma_S^4 \\ \vdots & \vdots & \ddots & \vdots \\ \sigma_S^4 & \sigma_S^4 & \dots & \sigma_S^2 + \sigma_S^4 \end{bmatrix} \tag{37}$$

By substituting the expressions in Eqs. (37) and (36) in to Eq. (31), the SNR of SIMO receiver output can be calculated as

$$\mathrm{SNR} = \frac{\underline{\tilde{\omega}}^T R_s \ \underline{\tilde{\omega}}}{\sigma_N^2 + M\sigma_N^4} \tag{38}$$

where $\underline{\tilde{\omega}} = \frac{\underline{\omega}}{||\underline{\omega}||}$ is the normalized gain vector. In order to obtain the gain vector maximizing the output SNR, Eq. (38) can be differentiated with respect to $\underline{\tilde{\omega}}$ to obtain the following gain vector after some algebraic simplifications:

$$\underline{\tilde{\omega}}_{opt} = \arg\max_{\underline{\tilde{\omega}}} \ (\mathrm{SNR}) = \arg\max_{\underline{\tilde{\omega}}} \ \left[\underline{\tilde{\omega}}^T R_s \ \underline{\tilde{\omega}}\right] = \underline{q}_1 \tag{39}$$

where $\underline{q}_1$ is the eigenvector corresponding to the largest eigenvalue in the R_s matrix. Given that all elements of the R_s (Eq. (37)) are positive and the sum of all rows is equal, it can be shown that, based on the Perron-Frobenius theorem [54], the largest eigenvalue of R_s is equal to this shared row-sum, and that $\underline{q}_1$ is a unit vector (i.e., $\underline{q}_1 = [1, \ 1, \dots 1]$). Incorporating this unit gain vector (hence the name EGC) in SIMO structures maximizes the output SNR suboptimally and is called EGC. By substituting $\underline{\tilde{\omega}}_{opt}$ in Eq. (38), the maximum SNR in SIMO structures benefiting from M separate receivers (each with aperture area of A/M) installed at different spatial positions (on a smartphone, for example) can be obtained as

$$\mathrm{SNR}_{\mathrm{EGC}} = \frac{\lambda_1}{\sigma_N^2 + M\sigma_N^4} = \frac{M\sigma_S^4 + \sigma_S^2}{\sigma_N^2 + M\sigma_N^4} \tag{40}$$

where $\lambda_1 = M\sigma_S^4 + \sigma_S^2$ is the largest[10] eigenvalue of R_s. As shown, increasing the number of branches (M) increases the SNR of the received signal and hence the communication range of the VLC link. However, the unnecessary increase in M will increase the hardware complexities and the final cost of the receiver without leading to further increase in the received SNR. The received SNR (Eq. (40)) is dependent on the fourth power of the standard deviation of the output data signal of each link. In other words, the required number of links to obtain the desired received SNR can be reduced by increasing the aperture area of the PD array employed in each link of the receiver. However, as previously explained, this increase in the active detection area of each link will also increase the time delay spread present in the channel impulse response of the corresponding link, specifically in vibrant VLC links.

C. Performance Analysis of SIMO-OGC VLC Receivers

In the subsection, the BER performance of SIMO-OGC system is assessed using the SPA method presented in Section VI. In order to obtain the analytical expression for the BER performance, the expressions associated with q+ and q- in the SPA method are modified as follows:

$$\phi_Y(s) = \frac{1}{2^L} \sum_{b_{-1},..,b_{-L}} \int_0^\infty \phi_{Y|(b_{-1},..,b_{-L},\tilde{H}=\tilde{h})}(s) f_{\tilde{H}}(\tilde{h}) \mathrm{d}\tilde{h} \tag{41}$$

$$\begin{aligned} \phi_{Y|(b_{-1},..,b_{-L},\tilde{H}=\tilde{h})}(s) &= E\left\{e^{sY}|(b_{-1},..,b_{-L},\tilde{H}=\tilde{h})\right\} \\ &= \sum_{i=0}^{M-1} \exp\left[(m_{y_i}(0) + (n_{b_i} + n_{d_i})T_b)\left(\exp(\omega_i s) - 1\right)\right] \end{aligned} \tag{42}$$

$$\phi_{Y,0}(s) \triangleq \phi_Y(s)|_{\text{Bit 0 is sent i.e., } (b_k=0|_{k=0})} \tag{43}$$

$$\phi_{Y,1}(s) \triangleq \phi_Y(s)|_{\text{Bit 1 is sent i.e., } (b_k=1|_{k=0})} \tag{44}$$

$$\begin{aligned} q_+(\nu_{th}) &\triangleq \Pr(Y > \nu_{th}|zero) \approx \frac{\exp\left[\Psi_0(s_0)\right]}{\sqrt{2\pi\Psi_0''(s_0)}} \\ q_-(\nu_{th}) &\triangleq \Pr(Y \leq \nu_{th}|one) \approx \frac{\exp\left[\Psi_1(s_1)\right]}{\sqrt{2\pi\Psi_1''(s_1)}} \\ \Psi_0(s) &\triangleq \ln\left[\phi_{Y,0}(s)\right] - s\nu_{th} - \ln|s| \\ \Psi_1(s) &\triangleq \ln\left[\phi_{Y,1}(s)\right] - s\nu_{th} - \ln|s| \end{aligned} \tag{45}$$

Finally, using SPA, the system BER can be obtained as $BER = \frac{1}{2}\left[q_+(\nu_{th}) + q_-(\nu_{th})\right]$.

X. Results and Discussion

The performance of the designed prototype is investigated using the optimal MSD detection algorithm and DF-APA adaptive symbol detection algorithm. The prototype designed in this study makes use of symbol by symbol detection (SBSD) while MSD and DF-APA improve BER performance in the VLC link through additional computation. The performance of the SBSD detector is also evaluated. For this purpose,

[10]Lemma: Let F be a matrix with positive entries, then, from the Perron-Frobenius Theorem [54], it follows that the largest eigenvalue of F is bounded between the lowest and the biggest sum of a row. Since in matrix R_s both are equal to the same value, the maximum eigenvalue of R_s must be equal to this common row sum value, and therefore, $\lambda_1 = M\sigma_S^4 + \sigma_S^2$.

using the SPA and the empirically derived vibrant channel impulse response and analytical relations in Section VI, the BER is calculated to examine destructive effects of vibration in detecting information by the VLC system. The SIMO structure in Section IX is also evaluated to improve the performance of the designed VLC system in vibrant VLC links. The use of optimal gain combining (OGC) significantly improved the performance of SBSD detectors in vibrant VLC links.

Table IV shows details of computational and memory complexities for three detection methods at a high level. SBSD is a baseline approach in our prototype in which each received symbol can be detected without any computational or memory cost. On the other end of the design spectrum, MSD detection method allows optimal detection of any N-bit block at the expense of an increase in the exponential time and linear memory complexities of SISO structures. The adaptive filtering technique DF-APA, finds a middle-ground by attaining linear time and memory complexities with some degradation of BER. In our evaluation, we aim to quantify this degradation too. By using the empirical channel impulse response of our prototype VLC link (in Fig. 7), we simulate SBSD, MSD and DF-APA. Table V summarizes key system parameters in the simulation, including the transmitter and receiver specifications.

1000X BER Improvement is Possible: By employing the MSD optimal detector in the receiver, we investigate the effect of increasing the window length N on improving the performance of the vibrating receiver at a bit rate of 20 Mbps. Since the highest detrimental ISI effects occur at this bit rate, we choose this particular bit rate for evaluation. Moreover, we are mainly interested in the performance of the MSD optimal detector in improving the detection efficiency under the worst conditions which in our case happens at 20 Mbps over 7.1 m distance. As shown in Fig. 12(a), increasing the window length in the MSD detector from N=2 to N=7 significantly decreases the average BER. Further increases in the window length ($N \geq 8$) have no notable effect on the performance and merely increases the computational complexity and the required buffer for storage of received signal symbols while delaying the decisions on the most probable transmitted N-bit.

TABLE V
SYSTEM PARAMETERS USED IN SIMULATIONS.

Coefficient	Value
Responsivity at $\lambda = 445$ nm, $\mathcal{R}$ (Fig. 4)	0.13
$\{G_{TIA}, G_{HPF}, G_{WBA}\}$ (Fig. 3)	$\{25, 2.57, 4001\}$
Quantum efficiency, η_Q	0.7
HPF elimination factor, η_E	10^{-6}
Electronic bandwidth, B (Eq. (2))	20.16 MHz
Optical blue filter bandwidth (Full Width Half Max), $\triangle\lambda$ (Fig. 5(b))	40 ± 8 nm
Optical filter transmissivity at $\lambda = 445$ nm, T_F (Fig. 5(b))	0.76
Dark current, I_{dc} at $\mathrm{V_B} = 18V$	80 μA
Transmission bit rate, $\mathrm{R_b}$	20 Mbps
Center-to-center LoS distance between transmitter and receiver	7.1 m
Channel memory, L	7
$\{\lambda_\mathrm{F}, \theta_\mathrm{F}\}$ [55]	$\{6.472, 6\}$

Adaptive Filtering Attains Near-Optimal BER: To understand if adaptive symbol detection will suffice, we, in Fig 12.(b), compare the performance of the DF-APA suboptimal detector and the optimal detector MSD in minimizing the detrimental ISI effects caused by the vibrations as well as in increasing the average BER at a bitrate of 20 Mbps. Moreover, we study the effect of the number of tap weights employed in the FF and FB filters in DF-APA (Fig. 12(b)) on improving the system performance. We used step size μ=0.0005 to plot the BER diagrams associated with the DF-APA detector. As shown in Fig. 12(b), DF-APA is able to achieve a performance close to that of the MSD optimal detector with a window length N=4 by employing 6 tap weights in the FF filter (N_{FF}=6) and 3 tap weights in the FB filter (N_{FB}=3) at a much lower computational complexity. However, this performance improvement by DF-APA requires accessing at least 1,000-bit training sequence (for a step size μ=0.0005) in the receiver.

An appropriate step size is critical for DF-APA detector in order to attain a good convergence speed and stability. Fig. 12(c) illustrates the relationship between the Mean Squared Error (MSE) by DF-APA and training sequence (d_k in training mode and $\tilde{d}_k$ in tracking mode) length in both training and tracking modes, where the number of gain taps in the detector's FF and FB filters are 6 and 3, respectively. To depict the learning curve, the expression $J(n) = |d_k - \hat{d}_k|^2$ in the training mode and $J(n) = |\tilde{d}_k - \hat{d}_k|^2$ in the tracking mode are computed from the detector's output, and after 1,000 times of running, the mean value of the results are obtained. As seen, $J(n)$ converges after about 1,500 iterations of updating the filter coefficients $\underline{\omega}$(n). Looking at various step sizes, the higher the step size (red and purple curves), the faster DF-APA finds the best coefficient configuration for symbol detection. However, higher step sizes may cause the filter going into potentially unstable operation. Fig. 12(c) shows that for step sizes $\mu \leq 0.01$ the DF-APA filter is stable. In particular, after about 300 iterations, all step sizes in both modes result in sufficient improvement in the learning curve and converge.

A key insight from the results is that DF-APA attains very fast learning of the VLC channel in about 1,500 iterations. This translates to roughly $N_{FF}+N_{FB}\times$1,500 arithmetic operations for a converged training. In a typical CPU with GHz clock frequencies, this could be done in the order of microseconds. Including the operating system delays, DF-APA can easily re-learn the tap weight coefficients in several milliseconds – making it possible to handle mobility in the receiver. Assuming that the receiver moves due to human movements, for instance within an office, the changes in the VLC channel's response will easily be handled by the DF-APA approach, because its microsecond re-learning timescale will be significantly smaller than human movement timescale in 100s of milliseconds.

Real-Time Data Transmission: We transmitted a 512 $\times$ 512 black-white image via our VLC system with a vibrant receiver. The distance was set to 7.1 m and the bit rate was 20 Mbps. Fig. 13(a), (b) and (c) show the received image quality in these experiments using the receivers SBSD, DF-APA, and MSD, respectively. We used MSD with a window length of N=4, and DF-APA method with buffers N_{FF}=6 and N_{FB}=3.

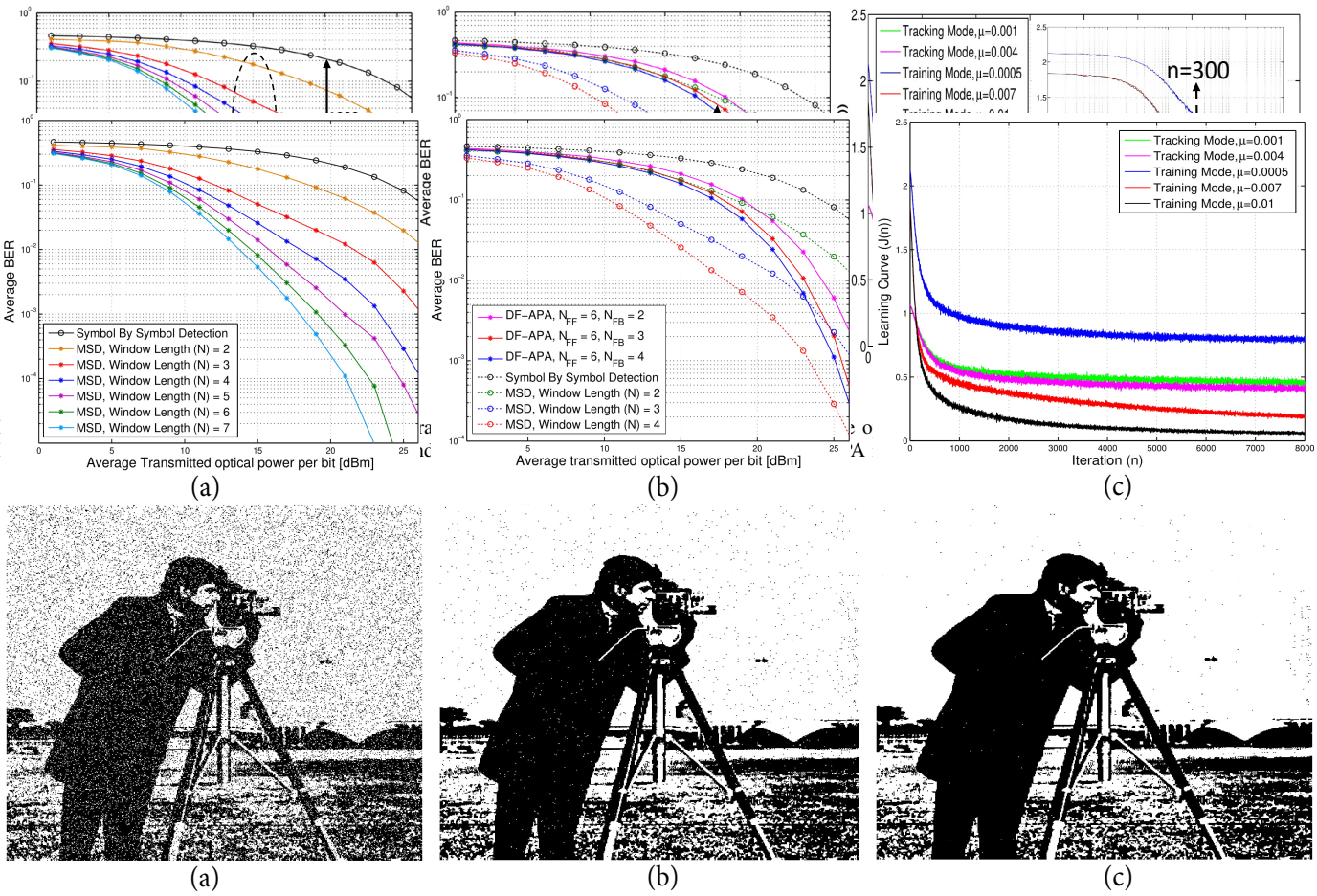

Fig. 13. Real-time data transmission via the VLC link: (a) Prototype's reception quality (SBSD); (b) Suboptimal DF-APA detection ($\mathbf{N_{FF}}$=6, $\mathbf{N_{FB}}$=3); (c) Optimal MSD (N=5).

As shown, the quality of the received signal using the DF-APA detector is not significantly different compared to that of the MSD detector, but the computational complexity and the computing time requirement for the former are considerably

SIMO with Gain Combining is Effective in Tackling the Delay Spread of the Vibrant Links: Fig. 14 evaluates and compares the performance of SIMO-OGC structures with SISO structures using the analytical relations derived for the system

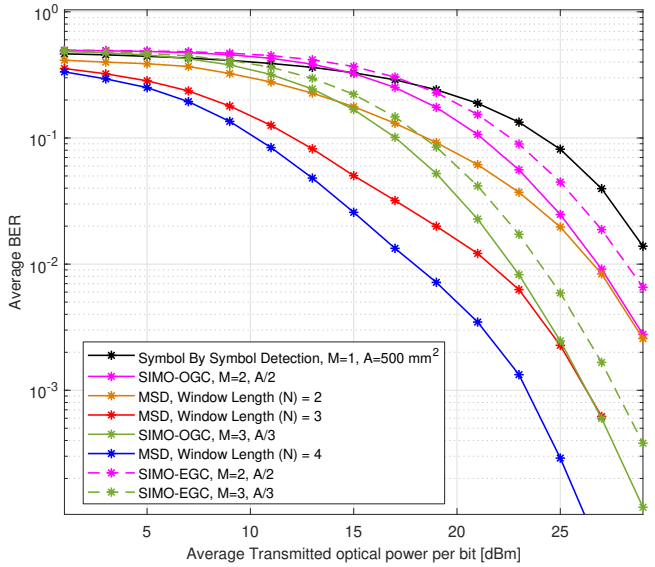

Fig. 14. Performance analysis and comparison of a 20 Mbps vibrant SIMO-OGC VLC receiver with $M = 2$ and $M = 3$ reception links.

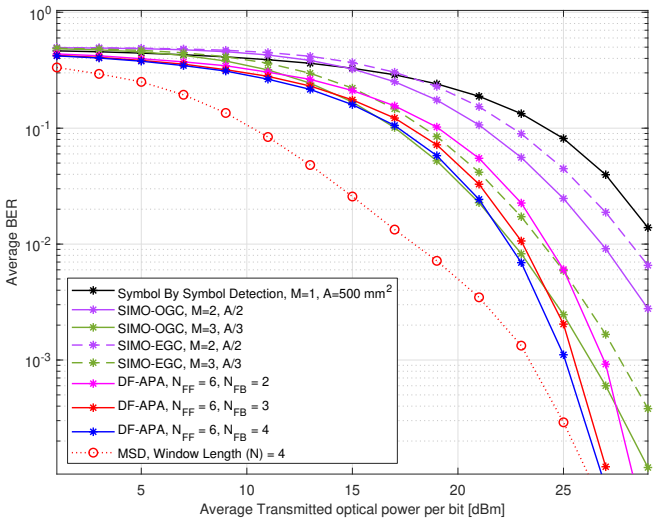

Fig. 15. Performance comparison of a 20 Mbps vibrant time-diverse DF-APA receivers and receiver diversity with optimal gain combination acquiring $M = 2$ and $M = 3$ reception links.

BER based on the SPA method described in Sections VI and IX. The comparison assumes the sum of all the receiving apertures in the SIMO structure is equal to the total active detection area of the SISO link amounting to A=500mm^2. As a result, the aperture area for each of the M separate links in the SIMO structure is A/M. As shown, the SIMO schemes featuring 2 and 3 receivers (with each receiver having an aperture area of $A/2$ and $A/3$, respectively) significantly outperform the SISO structure (with an active detection area of A), particularly at high SNR values. This indicates that employing more links with smaller aperture areas (such that the total active detection area remains unchanged) can lead to the optimum performance, particularly at high SNRs.

An optimum BER performance was obtained in both SIMO schemes with 2 and 3 separate receivers, which previously could only be achieved through the MSD method with window length (i.e., N) of 2 and 3 at an exponential computational complexity. This improved performance can be intuitively explained by the fact that a large aperture area in a single link further increases the channel delay spread in vibrant VLC links. As a result, by dividing the total active detection area of the single receiver between M separate spatial links (i.e. each with an aperture area of A/M), the interference caused by the delayed photons due to the previously transmitted bits is reduced, consequently improving the performance of the system in SIMO-OGC schemes. Furthermore, our numerical results indicate that utilizing receiver diversity with sub-optimal SIMO-EGC can be practically interesting, due to its lower implementation complexity and its close performance to OGC. Fig. 15 compares the performance of the time-diverse DF-APA and the spatially diverse SIMO-OGC receivers. As shown, DF-APA receivers can lead to similar performance improvements comparing to SIMO-OGC. However, when using the DF-APA, there is a trade-off between the BER and the time cost of the detector adaptation, and its bit buffering needs (Fig. 13(a)) and receiver diversity with OGC can be considered a proper and alternative solution to this trade-off.

XI. Conclusion

A visible light communication (VLC) system capable of information communication with a reception bit rate of 20 Mbps was designed in a communication range of 7.1 m. By presenting a systematic approach to achieve the maximum reception bit rate in the designed prototype, the trade-off between active detection area of avalanche photodiodes (APDs), stability of the receiver circuit and eventually the maximum communication range and the bandwidth supported by the VLC receiver were investigated. Both vibrant and non-vibrant VLC links were then considered. Deploying the designed prototype in both links, the destructive effects of intense vibrations in the physical structure of the VLC systems on the channel impulse response and quality of received signal were evaluated.

The performance of the designed VLC receiver in detecting information communicated by a stationery visible light transmitter was investigated using the symbol by symbol detector (SBSD) in both vibrant and non-vibrant VLC links. To this end, analytical expressions were obtained for the system BER using the saddle point approximation and empirically derived vibrant channel impulse response. Utilizing the resulting relations, the destructive vibration effects on detecting information by the VLC system were studied at different transmission bit rates. According to the results, an increase in the bit rate causes an increase in the probability of bit error resulting from intersymbol interference (ISI) and delay spread in vibrant links. In other words, as the bit rate increases, the bit time approaches the delay spread in the vibrant channel impulse response. This, in turn, causes an increase in the uncertainty of symbol detection leading to a decrease in the performance of the system and an increase in BER.

To reduce ISI and to adapt to the time-varying nature of vibrant VLC links, optimal MSD and suboptimal DF-APA detectors were designed and employed. The use of optimal MSD detectors significantly improved the performance in the vibrant VLC links at the expense of exponential time complexity and highly nonlinear nature of the MSD algorithm. Utilizing the suboptimal adaptive DF-APA detector, a performance close to that under optimal conditions can be obtained in the vibrant links but with polynomial time costs. We also explored receiver spatial diversity combining techniques. To this end, we evaluated SIMO designs equipped with a novel Optimal Gain Combination (OGC) detection algorithm which takes advantage of the intrinsic spatial diversity of the VLC receivers with large detection area. We also observed that relying on the extra spatial diversity provided by the SIMO reception is crucial to achieve the targeted reliability level in vibrant VLC links.

A key outcome of our work is the possibility of attaining VLC receivers with large reception areas which may be designed conformal to receiver's surface. Future work could explore the benefit of using more computation and learning to improve the performance of mobile VLC receivers. Using single photon avalanche photodiodes (SPAD) instead of avalanche photodiodes (APD) may prove to attain higher communication ranges at indoor environments with low-level light intensity.

Appendix A
Saddle-point Approximation of BER

Following Helstrom [40], G. Einerson has derived a numerically simple approximation to the cumulative probability distribution of a continuous stochastic variable with density $p(x)$ [41]. Let $q_+(\alpha)$ denote the upper tail

$$q_+(\alpha) = \int_{\alpha}^{\infty} p(x)dx \tag{46}$$

and

$$q_-(\alpha) = \int_{-\infty}^{\alpha} p(x)dx \tag{47}$$

the lower tail of the probability distribution. The bilateral Laplace transform of $p(x)$ can be expressed in term of the moment generating function as

$$\Psi(-s) = \int_{-\infty}^{\infty} e^{-sx}dx \tag{48}$$

The probability density $p(x)$ is equal to the inverse integral

$$p(x) = \frac{1}{2\pi j}\int_{c-j\infty}^{c+j\infty} \Psi(-s)e^{sx}ds \tag{49}$$

where c is in the convergence region of the transform.

By replacing $p(x)$ in (46) with (49) and choosing the contour of integration such that $c < 0$ to guarantee convergence of the integral, the resulting lower tail is

$$q_+(\alpha) = \frac{1}{2\pi j}\int_{c-j\infty}^{c+j\infty} \frac{e^{s\alpha}}{s}\Psi(-s)ds.$$

Changing the integration variable from $-s$ to s gives

$$q_+(\alpha) = \frac{1}{2\pi j}\int_{c-j\infty}^{c+j\infty} \frac{e^{-s\alpha}}{s}\Psi(-s)ds; \quad c > 0. \tag{50}$$

The parameter c is chosen to be s for which the integrand is minimal. It turns out $s = s_0$ corresponds to a saddle-point in complex plane, hence the name of the method. The integrand in terms of a 'phase' function $\psi(s)$ is defined by

$$\exp[\psi(s)] = |s|^{-1}\exp(-s\alpha)\Psi(s) \tag{51}$$

The function $\psi(s)$ is expanded in a Taylor series around the point $s = s_0$:

$$\psi(s) = \psi(s_0) + \frac{1}{2}\psi^{''}(s_0)(s - s_0)^2 + \dots \tag{52}$$

The first derivative does not appear since $s = s_0$ is an extremum of $\psi(s)$.

Substitution of (52) into (50) and neglecting higher-order terms yields the saddle-point approximation:

$$\begin{aligned} q_-(\alpha) &\approx \frac{1}{2\pi}\exp[\psi(s_0)]\int_{-\infty}^{\infty}\exp\left[-\frac{1}{2}\psi^{''}(s_0)y^2\right]dy \qquad (53)\\ &= \left[2\pi\psi^{''}(s_0)\right]^{-1/2}\exp[\psi(s_0)] \end{aligned}$$

The parameter s_0 is the value of s for which $\psi(s)$ has a minimum. It is equal to the positive root of the equation:

$$\psi^{'}(s) = 0 \tag{54}$$

For the lower tail, analogously to (50),

$$q_-(\alpha) = \frac{-1}{2\pi j}\int_{c-j\infty}^{c+j\infty} \frac{e^{-s\alpha}}{s}\Psi(s)ds \tag{55}$$

with $c < 0$. Expansion of $\psi(s)$ in a Taylor series and integration gives:

$$q_-(\alpha) \approx [2\pi\psi^{''}(s_1)]^{-1/2}\exp[\psi(s_1)] \tag{56}$$

with s_1 equal to the negative root of (54).

REFERENCES

[1] P. Nabavi and M. Yuksel, "Conformal VLC receivers with photodetector arrays: Design, analysis and prototype," in *ICC 2019 - 2019 IEEE International Conference on Communications (ICC)*, May 2019, pp. 1–7.

[2] H. Ma, L. Lampe, and S. Hranilovic, "Coordinated broadcasting for multiuser indoor visible light communication systems," *IEEE Transactions on Communications*, vol. 63, no. 9, pp. 3313–3324, 2015.

[3] J. M. Kahn and J. R. Barry, "Wireless infrared communications," *Proceedings of the IEEE*, vol. 85, no. 2, pp. 265–298, 1997.

[4] X. Zhu and J. M. Kahn, "Free-space optical communication through atmospheric turbulence channels," *IEEE Transactions on Communications*, vol. 50, no. 8, pp. 1293–1300, 2002.

[5] H. Willebrand and B. S. Ghuman, *Free space optics: enabling optical connectivity in today's networks*. SAMS Publishing, 2002.

[6] M. V. Jamali, P. Nabavi, and J. A. Salehi, "MIMO underwater visible light communications: Comprehensive channel study, performance analysis, and multiple-symbol detection," *IEEE Transactions on Vehicular Technology*, vol. 67, no. 9, pp. 8223–8237, Sep. 2018.

[7] M. V. Jamali, A. Mirani, A. Parsay, B. Abolhassani, P. Nabavi, A. Chizari, P. Khorramshahi, S. Abdollahramezani, and J. A. Salehi, "Statistical studies of fading in underwater wireless optical channels in the presence of air bubble, temperature, and salinity random variations," *IEEE Transactions on Communications*, vol. 66, no. 10, pp. 4706–4723, Oct 2018.

[8] P. Nabavi, A. F. M. S. Haq, and M. Yuksel, "Empirical modeling and analysis of water-to-air optical wireless communication channels," in *2019 IEEE International Conference on Communications Workshops (ICC Workshops)*, May 2019, pp. 1–6.

[9] P. Gupta and P. R. Kumar, "The capacity of wireless networks," *IEEE Transactions on Information Theory*, vol. 46, no. 2, pp. 388–404, March 2000.

[10] I. F. Akyildiz, X. Wang, and W. Wang, "Wireless mesh networks: a survey," *Computer Networks*, vol. 47, no. 4, pp. 445 – 487, 2005.

[11] M. Ayyash, H. Elgala, A. Khreishah, V. Jungnickel, T. Little, S. Shao, M. Rahaim, D. Schulz, J. Hilt, and R. Freund, "Coexistence of WiFi and LiFi toward 5G: Concepts, opportunities, and challenges," *IEEE Communications Magazine*, vol. 54, no. 2, pp. 64–71, February 2016.

[12] M. Khan and M. Yuksel, "Maintaining a free-space-optical communication link between two autonomous mobiles," in *2014 IEEE Wireless Communications and Networking Conference (WCNC)*, April 2014, pp. 3154–3159.

[13] A. M. Cailean and M. Dimian, "Current challenges for visible light communications usage in vehicle applications: A survey," *IEEE Communications Surveys Tutorials*, vol. 19, no. 4, pp. 2681–2703, Fourthquarter 2017.

[14] Pure Lifi corporate. chief executive scientist: Professor Harald Haas FRSE. [Online]. Available: https://purelifi.com/lifi-products/

[15] A. Liu, J. Li, G. Shen, C. Sun, L. Li, and F. C. Zhao, "Enabling low-power duplex visible light communication," *CoRR*, vol. abs/1801.09812, 2018.

[16] M. Mi Zhou, M. Lun Zhang, and Y. Gan Zhang, "Design and implementation of long distance visible light communication system based on embedded ARM platform," *Applied Mechanics and Materials*, vol. 462-463, pp. 643–646, 11 2013.

[17] Thorlabs. Part number: PDA36A2. [Online]. Available: https://www.thorlabs.com

[18] E. T. Won, D. Shin, D. Jung, Y. Oh, T. Bae, H.-C. Kwon, C. Cho, J. Son, D. O'Brien, T.-G. Kang, and T. Matsumura, "IEEE P802.15 working group for wireless personal area networks (wpans): Visible light communication: Tutorial," 2018.

[19] S. Rajagopal, R. D. Roberts, and S. Lim, "IEEE 802.15.7 visible light communication: Modulation schemes and dimming support," *IEEE Communications Magazine*, vol. 50, no. 3, pp. 72–82, March 2012.

[20] H. Le Minh, D. O'Brien, G. Faulkner, L. Zeng, K. Lee, D. Jung, and Y. Oh, "80 Mbit/s visible light communications using pre-equalized white LED," in *Optical Communication, 2008. ECOC 2008. 34th European Conference on*. IEEE, 2008, pp. 1–2.

[21] H. L. Minh, D. O'Brien, G. Faulkner, L. Zeng, K. Lee, D. Jung, and Y. Oh, "High-speed visible light communications using multiple-resonant equalization," *IEEE Photonics Technology Letters*, vol. 20, no. 14, pp. 1243–1245, July 2008.

[22] J. Grubor, S. C. J. Lee, K.-D. Langer, T. Koonen, and J. W. Walewski, "Wireless high-speed data transmission with phosphorescent white-light LEDs," in *Optical Communication-Post-Deadline Papers (published 2008), 2007 33rd European Conference and Exhibition of*. VDE, 2007, pp. 1–2.

[23] S. Park, D. Jung, H. Shin, D. Shin, Y. Hyun, K. Lee, and Y. Oh, "Information broadcasting system based on visible light signboard," *Proceedings of the Wireless and Optical Communications, Montreal, QC, Canada*, vol. 30, 2007.

[24] T. Koonen, "Indoor optical wireless systems: Technology, trends, and applications," *Journal of Lightwave Technology*, vol. 36, no. 8, pp. 1459–1467, April 2018.

[25] G. P. Agrawal, *Fiber-optic communication systems*. John Wiley & Sons, 2012, vol. 222.

[26] Thorlabs. Part number: FDS1010. [Online]. Available: https://www.thorlabs.com

[27] J. G. Graeme, *Photodiode amplifiers: Op amp solutions*. McGraw-Hill New York, 1996.

[28] C. B. Yahya, "Design of wideband low noise transimpedance amplifiers for optical communications," in *Proceedings of the 43rd IEEE Midwest*

Symposium on Circuits and Systems (Cat.No.CH37144), vol. 2, 2000, pp. 804–807 vol.2.
[29] F. Capasso, "Physics of avalanche photodiodes," in *Semiconductors and semimetals*. Elsevier, 1985, vol. 22, pp. 1–172.
[30] P. Nabavi and M. Yuksel, "Performance analysis of air-to-water optical wireless communication using SPADs," in *Proceedings of 2019 IEEE Global Communications Conference (GLOBECOM)*, February 2019.
[31] F. He, R. Ribas, C. Lahuec, and M. Jézéquel, "Discussion on the general oscillation startup condition and the barkhausen criterion," *Analog Integrated Circuits and Signal Processing*, vol. 59, no. 2, pp. 215–221, 2009.
[32] H. Jiang and P. K. L. Yu, "Equivalent circuit analysis of harmonic distortions in photodiode," *IEEE Photonics Technology Letters*, vol. 10, no. 11, pp. 1608–1610, Nov 1998.
[33] A. Waters, *Active Filter Design*. Springer, 1991.
[34] L. P. Huelsman, *Active and passive analog filter design: An introduction*. McGraw-Hill, 1993.
[35] S. Mardani, A. Khalid, F. M. J. Willems, and J. P. Linnartz, "Effect of blue filter on the SNR and data rate for indoor visible light communication system," in *2017 European Conference on Optical Communication (ECOC)*, Sept 2017, pp. 1–3.
[36] S. W. Wang, F. Chen, L. Liang, S. He, Y. Wang, X. Chen, and W. Lu, "A high-performance blue filter for a white LED-based visible light communication system," *IEEE Wireless Communications*, vol. 22, no. 2, pp. 61–67, April 2015.
[37] J. T. Broch, *Mechanical Vibration and Shock Measurements*. Brel & Kjr, 1984.
[38] Z. Ghassemlooy, W. Popoola, and S. Rajbhandari, *Optical wireless communications: system and channel modelling with Matlab®*. CRC Press, 2012.
[39] A. Chizari, M. V. Jamali, S. Abdollahramezani, J. A. Salehi, and A. Dargahi, "Visible light for communication, indoor positioning, and dimmable illumination: A system design based on overlapping pulse position modulation," *Optik-International Journal for Light and Electron Optics*, vol. 151, pp. 110–122, 2017.
[40] G. Einarsson, *Principles of Lightwave Communications*. New York: Wiley, 1996.
[41] R. M. Gagliardi and S. Karp, *Optical Communications*. New York: Wiley, 1995.
[42] M. Jazayerifar and J. A. Salehi, "Atmospheric optical CDMA communication systems via optical orthogonal codes," *IEEE Transactions on Communications*, vol. 54, no. 9, pp. 1614–1623, Sept 2006.
[43] T. Komine and M. Nakagawa, "Fundamental analysis for visible-light communication system using LED lights," *IEEE Transactions on Consumer Electronics*, vol. 50, no. 1, pp. 100–107, Feb 2004.
[44] X. Zhu and J. M. Kahn, "Performance bounds for coded free-space optical communications through atmospheric turbulence channels," *IEEE Transactions on Communications*, vol. 51, no. 8, pp. 1233–1239, Aug 2003.
[45] N. D. Chatzidiamantis, G. K. Karagiannidis, and M. Uysal, "Generalized maximum-likelihood sequence detection for photon-counting free space optical systems," *IEEE Trans. Commun.*, vol. 58, no. 12, pp. 3381–3385, 2010.
[46] M. L. B. Riediger, R. Schober, and L. Lampe, "Fast multiple-symbol detection for free-space optical communications," *IEEE Transactions on Communications*, vol. 57, no. 4, pp. 1119–1128, April 2009.
[47] J. G. Proakis and M. Salehi, *Digital communications*. McGraw-Hill, 2008.
[48] T. Rappaport, *Wireless Communications: Principles and Practice, 2nd Edition*. Prentice Hall PTR, 2002.
[49] S. L. Gay and S. Tavathia, "The fast affine projection algorithm," in *1995 International Conference on Acoustics, Speech, and Signal Processing*, vol. 5, May 1995, pp. 3023–3026 vol.5.
[50] A. H. Sayed, *Fundamentals of Adaptive Filtering*. Wiley, June 2003.
[51] Y. V. Zakharov, "Low-complexity implementation of the affine projection algorithm," *IEEE Signal Processing Letters*, vol. 15, pp. 557–560, 2008.
[52] B. Farhang-Boroujeny, *Adaptive filters: theory and applications*. John Wiley & Sons, 2013.
[53] G. H. Golub and C. F. Van Loan, *Matrix computations*. JHU Press, 2012, vol. 3.
[54] E. Seneta, *Non-Negative Matrices and Markov Chains*. Berlin,Germany: Springer, 2006.
[55] K. Kiasaleh, "Performance of APD-based, PPM free-space optical communication systems in atmospheric turbulence," *IEEE Transactions on Communications*, vol. 53, no. 9, pp. 1455–1461, Sept 2005.